Article

Not peer-reviewed version

Moiré Superconductivity and the Roeser-Huber Formula

Michael Rudolf Koblischka * and Anjela Koblischka-Veneva

Posted Date: 9 June 2023

doi: 10.20944/preprints202306.0688.v1

Keywords: Moiré Superconductors; twisted bilayer graphene; WSe2; superconducting transition temperature; Roeser-Huber formula

Article

Moiré Superconductivity and the Roeser-Huber Formula

Michael Rudolf Koblischka * and Anjela Koblischka-Veneva

Saarland University, Experimental Physics, P. O. Box 151150, D-66041 Saarbrücken, Germany; a.koblischka@gmail.com

* Correspondence: m.koblischka@gmail.com or m.koblischka@ieee.org

Abstract: Moiré superconductivity represents a new class of superconducting materials since the discovery of magic-angle twisted bi-layer graphene (tBLG), forming a Moiré lattice with a much bigger crystal parameter as the original crystallographic distance of graphene. Thus, changing the Moiré twist angle, Θ, leads to a variation of the superconducting properties and enables a new way of engineering 2D superconducting materials. Here, the details of the superconducting state of tBLG as function of charge carrier density, temperature and applied magnetic fields are reviewed. Furthermore, the influence of the top and bottom h-BN (hexagonal boron nitride) layer thickness on the resulting superconducting properties of the tBLG samples was demonstrated. Changing of the charge carrier density in the tBLG samples leads to the appearance of insulating, metallic and even ferromagnetic states, which separate several superconducting domes in the phase diagram (longitudinal resistance, R_{xx} as function of temperature T and charge carrier density, n). Following the basic ideas of Moiré superconductors, further works have considered tri-layer graphene (TLG), tBLG combined with WSe_2-layers as well as twisted, bi-layer WSe_2. Here, the experimental results obtained in the literature concerning superconductivity are reviewed with the focus on the experimentally determined superconducting transition temperatures, T_c, which were found to depend on the twist angle, the charge carrier density and the cover layer thickness. The differences between the layered high-T_c superconductors and the Moiré superconductors are summarized. The collected information is then used to apply the Roeser-Huber formalism to Moiré-type superconductivity in order to calculate the superconducting transition temperature, T_c, using only information of the crystal lattice and the electronic configuration. A first attempt using the Moiré lattice constant, a_M, and parameters similar to the layered high-T_c superconductors leads to T_c values being too high as compared to the experimental data. The reasons for this result are discussed in detail. To account for the different charge carrier densities in the experimental data sets and the low charge carrier mass demands that a new parameter labelled η must be introduced to the Roeser-Huber formalism serving as a correction factor to describe the several superconducting domes found in the phase diagram for a given Moiré angle. Doing so, the calculated data fit well to the correlation curve defined within the Roeser-Huber formalism.

Keywords: Moiré Superconductors; twisted bilayer graphene; WSe_2; superconducting transition temperature; Roeser-Huber formula

1. Introduction

Moiré superconductivity, which was first demonstrated experimentally in 2018, involves creating large, periodic superstructures in 2D materials as compared to the atomic scale. The first sample belonging to this new family of superconductors was found when stacking two graphene layers together with a small misalignment angle, $\Theta \sim 1.1°$, called also the magic angle [1,2]. This graphene stack is called twisted bilayer graphene or abbreviated tBLG [2,3]. The misalignment between the two graphene layers creates a Moiré pattern which has a spatial period, a_M, being a factor $1/\Theta$ larger than the unit cell on the atomic level. At the so-called magic angles, the Fermi velocity drops to zero, and the first magic angle is predicted to be $\Theta_{magic} \approx 1.1°$. Near this twist angle, the energy bands near charge

 doi:10.20944/preprints202306.0688.v1

neutrality, which are separated from other bands by single-particle gaps, become remarkably flat [4,5]. The typical energy scale for the entire bandwidth is about 5-10 meV. Experiments enabled the flatness of these bands to be confirmed by an high effective mass seen in quantum oscillations, and correlated insulating states at half-filling of these bands were observed [1], corresponding to $n = \pm n_s/2$ with $n = C \cdot V_g/e_0$ being the charge carrier density defined by the applied gate voltage V_g, C corresponds to the gate capacitance per unit area, and e_0 is the electron charge. Electrostatic doping the material away from these correlated insulating states enabled the observation of tunable zero-resistance states, which correspond to the presence of superconductivity. Very remarkably, the observed superconducting transition temperatures, T_c, can be several degrees K high.

Since these first experimental reports, superconductivity in tBLG has been observed in ambient conditions [6–10] and under pressure [3] by other authors in the literature as well, including various twist angles around the magic angle, various charge carrier densities, and different thicknesses of the hexagonal boron nitride (abbreviated h-BN) layers on top and bottom of the tBLG [10]. The superconducting properties, including the critical fields and the superconducting parameters κ, λ_L and ξ of these samples, are well documented including a classification of the Moiré superconductors as presented by Talantsev [11].

Furthermore, the superconductivity of a trilayer stack of graphene with a misalingment of $\pm 1.1^\circ$ was reported [12], in an ABC-type trilayer stack [13], and Arora et al. have combined the tBLG with a monolayer of WSe_2 additional to the h-BN layers [14]. The basic idea of Moiré superconductivity was further extended in a report of superconductivity in misaligned ($\Theta = 1^\circ$, 4°) double layers of WSe_2 [15], but the data provided concerning the superconducting properties of this system are much less convincing as compared to the other reports on tBLG as mentioned also in another recent review [16]. Similar detailed experiments concerning superconductivity on other types of twisted, bi-layered hexagonal lattice materials like stanene or borophene are still missing in the literature [17,18].

The appearance of several superconducting domes in the phase diagram (here, the resistivity is plotted color-coded as a function of temperature, $R(T)$, for various charge carrier densities, n) at different charge carrier concentrations was described by Lu et al. [6]. These superconducting domes, being quite similar to the doping diagram of the cuprate HTSc, are separated by metallic states, insulators and even ferromagnets. Thus, this topic is intensively investigated by band structure calculations [19–24] and gives rise to a continuously growing number of new experimental and theoretical aspects [25–49].

It is important to note here that Moiré patterns can be formed also in cases when different types of 2D-layered materials are stacked together, with or without angular misalignment, or between a 2D layer and a substrate [50,51]. As result, the resulting Moiré lattice parameter, a_M, may be considerably larger than the original atomic unit cells of any ingredient. Several details of the mathematics of Moiré patterns were already presented in Refs. [52–55]. Thus, the stacking of various 2D-layered materials offers a versatile new way to control superconductivity in layered 2D-systems ("Moiré-superconductors"), the full potential of which has been barely explored yet [56–61]. So, to further investigate this field and unleash more possibilities to find new materials with higher T_c's, a relatively simple calculation procedure which can be included in machine-learning approaches, see, e.g., Refs. [62–67], is extremely useful.

As the lattice constant of the Moiré pattern plays an important role for the observation of superconductivity, it is straightforward to follow this relation between superconductivity and the characteristic sample dimension in more detail. For high-temperature superconductors (HTSc), and later also for iron-based superconductors (IBS), fullerenes, elemental superconductors and metallic alloys, the Roeser-Huber fomula was developed to calculate the superconducting transition temperature, T_c. This approach only requires to find a characteristic length of the sample crystallography, x, and some knowledge about the electronic configuration [68–76]. All this information may be found in existing databases. Using the Roeser-Huber formalism, the T_c of several superconducting materials could be calculated with only a small error margin [74,76], and recently, the

 doi:10.20944/preprints202306.0688.v1

approach was even employed to predict T_c of metallic hydrogen with different crystal lattices [77]. In case of double-doped HTSc materials (e.g., the Cu-O-plane of $Bi_2Sr_2CaCu_2O_{8+\delta}$ (Bi-2212) doped by oxygen and by additional metal ions like Y or La), two characteristic doping patterns result, and the final T_c of the material is calculated as a Moiré-pattern of the two doping arrangements [70]. Thus, it is only straightforward to apply this calculation scheme to the real Moiré superconductors, where a clear crystallographic relation is defined by the orientation of the tBLG and by the unit cell of the tBLG itself.

In the present contribution, the existing literature concerning the superconducting properties with special emphasis on the transition temperatures of the various Moiré superconductors are reviewed, and the application of the Roeser-Huber formalism to Moiré superconductivity is presented including the introduction of a new parameter to account for the variations in charge carrier density.

This paper is organized as follows: In Section 2, some details of the fabrication steps of the tBLG samples are outlined and the resistance measurements performed to observe superconductivity in several superconducting domes are presented. Section 3 discusses the properties of the superconducting phase diagrams of the various Moiré superconductors presented in the literature. Then, in Section 4 the Roeser-Huber formalism as developed for HTSc is introduced. Section 5 discusses the calculation of the superconducting transition temperatures of the Moiré superconductors solely on the base of the electronic configuration and the respective Moiré parameters. Finally, Section 6 gives some conclusions and an outlook for future developments.

2. Materials and Methods

2.1. Moiré superlattices

Figure 1a presents a Moiré superlattice of two graphene layers (blue, red) tilted by an angle of 5° for clarity. The resulting lattice parameter, a_M, is indicated by a black line. In Ref. [12], also a tri-layer structure was presented with the top and bottom layers tilted by ±5° with respect to the center layer. This situation is depicted in Figure 1b.

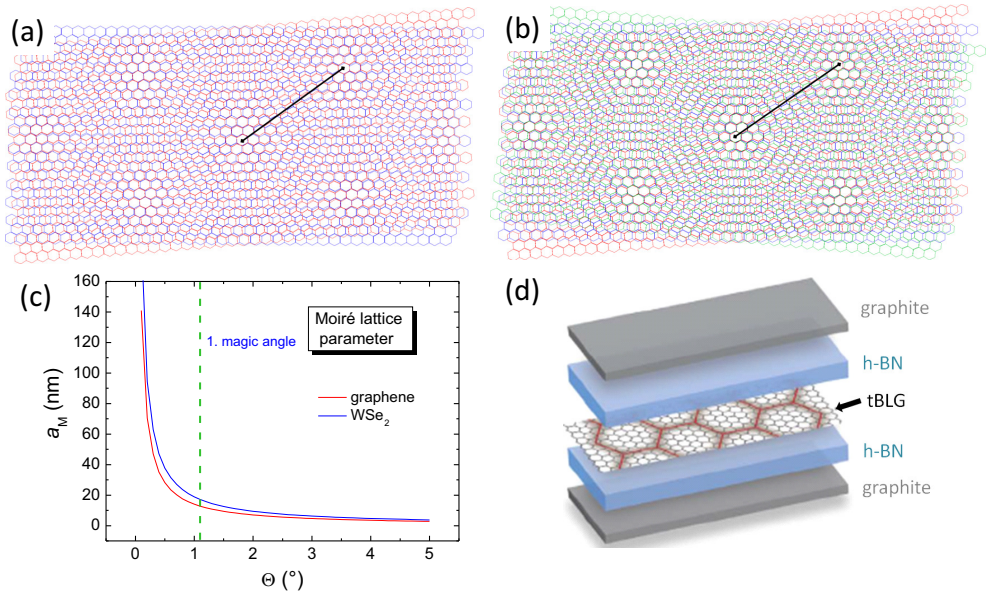

Figure 1. (**a**) Moiré pattern of two graphene layers (red, blue) tilted by 5°. This value was chosen for clarity. The black line indicates the resulting Moiré lattice parameter, a_M. (**b**) Moiré pattern of a tri-layer graphene system (red, blue, green) with the top and bottom layer tilted by ±5° with respect to the center layer. (**c**) Moiré lattice parameter, a_M, of graphene as function of the tilt angle, Θ. The first magic angle, 1.1°, is marked by a dashed green line (- - - -). (**d**) Schematic view of the various layers in a device for resistance measurement. Figure adapted from Ref. [3].

 doi:10.20944/preprints202306.0688.v1

The lattice parameter of graphene is $a_0^G = 0.246$ nm, and the one of WSe_2 is $a_0^{WSe_2} = 0.353$ nm [78]. Then, the possible Moiré patterns of two identical layers at an angle Θ have a periodicity according to

$$a_M = \frac{a_0}{2 \cdot \sin(\Theta/2)} \quad , \tag{1}$$

with a_M denoting the lattice constant of the Moiré superlattice (MSL). Figure 1c depicts the dependence of the Moiré lattice constant, a_M, as a function of Θ for graphene as well as for WSe_2.

The magic angle Θ_{magic} is given by [79]

$$\Theta_{\text{magic}} = \cos^{-1}\left(\frac{k^2 + 4kl + l^2}{2 \cdot (k^2 + kl + l^2)}\right) \quad , \tag{2}$$

with k, l being integers. The first magic angle, 1.1°, is indicated in Figure 1c by a dashed green line.

The accuracy achieved to determine the tilt angle of the graphene layers is typically ∼0.03° [10]; Stepanov et al. describe the twist homogeneity within a device as good as 0.01° per 10 μm [9]. Thus, the twist angles are well defined with only small experimental error.

2.2. Samples and resistance measurements

The superlattice density $n_s = 4/A$ was defined to be the density that corresponds to full-filling each set of degenerate superlattice bands, where $A \approx \sqrt{3}a^2/(2\Theta^2)$ is the area of the Moiré unit cell ($a = 0.246$ nm is the lattice constant of the underlying graphene lattice) and Θ is the twist angle. The electron density ($n_0 = A_0^{-1} \approx 10^{12}$ cm^{-2}, where A_0 is the area of the moiré unit cell) the observation of correlated states at all integer fillings of $\nu = n/n_0$ (where n denotes the gate-modulated carrier density), at Moiré band filling factors $\nu = 0, \pm1, \pm2, \pm...$

To measure the superconducting properties of tBLG by means of resistance measurements, a structure called device is fabricated using the tear-and-stack or cut-and-stack method encapsulating the tBLG between h-BN layers. This arrangement is then patterned into a Hall bar geometry with multiple leads using electron beam lithography and reactive ion-etching. The final device is placed on Si/SiO_2 substrate with an intermediate thick graphite layer serving as back gate. Another graphite layer on top serves for protection. This construction is required to prepare proper electric contacts to the sample. A schematic drawing of the arrangement of the various layers is given in Figure 1d and the device ready for measurement is given as an inset to Figure 2a.

Figures 2a and b present resistance measurements as a function of temperature for tBLG. In Figure 2a, the measured resistance, R_{xx}, being in the kΩ-range, is presented for two twist angles, 1.16° (M1) and 1.05° (M2) [2]. The inset shows the arrangement of sample and electric contacts ready for measurement. Figure 2b gives similar data from Ref. [6], but only for one angle (1.10°) and normalized to the resistance measured at 8 K. The different curves are obtained for various charge carrier densities, ranging between $+1.11 \times 10^{12}$ cm^{-2} to -1.73×10^{12} cm^{-2}. From this plot, it is obvious that the shape of the curves as well as the determined transition temperatures strongly vary with the charge carrier density. The variation of the charge carrier densities is achieved by tuning the gate voltage, which enables an extensive study of the phase diagram of the tBLG devices.

Preprints.org (www.preprints.org) | NOT PEER-REVIEWED | Posted: 9 June 2023 doi:10.20944/preprints202306.0688.v1

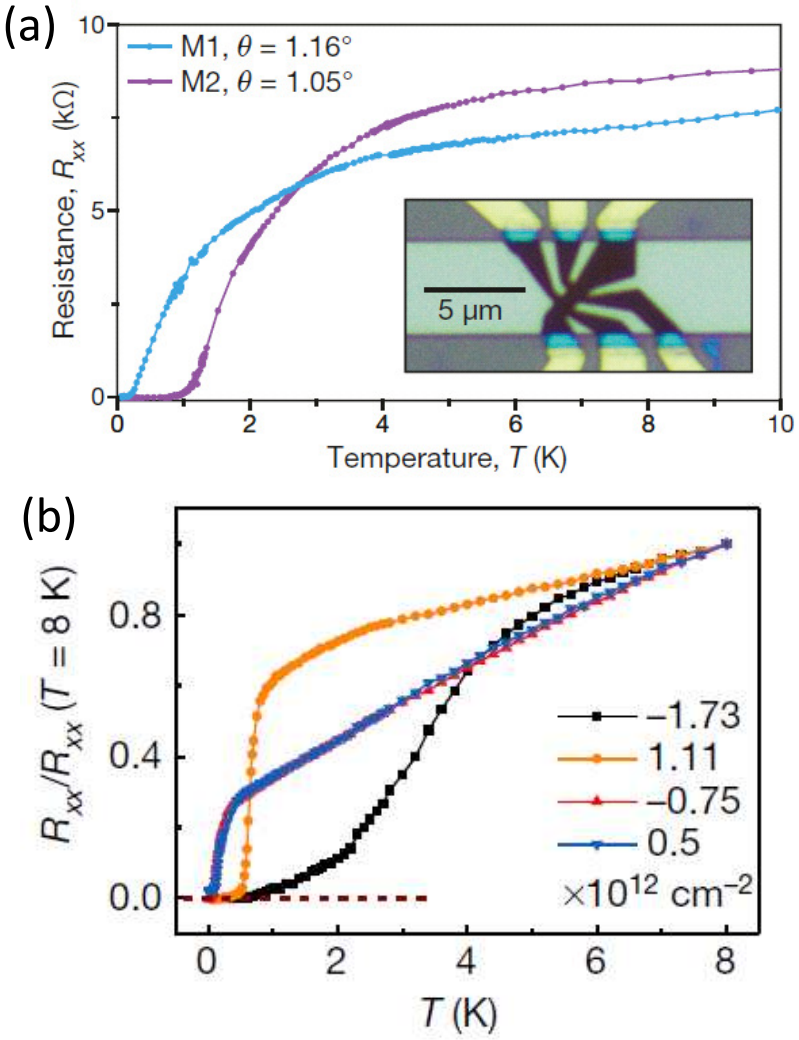

Figure 2. (**a**) Longitudinal resistance, R_{xx}, being in the kΩ-regime, measured by four-probe method in two devices M1 and M2 with twist angles of $\Theta = 1.16°$ and $\Theta = 1.05°$, respectively. The inset shows an optical image of device M1, including the main 'Hall' bar (dark brown), the electrical contacts (gold), the back gate (light green) and the SiO_2/Si substrate (dark grey). Reproduced with permission from Ref. [2]. (**b**) Longitudinal resistance at optimal doping of the superconducting domes as a function of temperature. The resistance is normalized to its value at 8 K. Note that data points for $n = -7.5 \times 10^{11}$ cm^{-2} are overlaid by the data points for $n = 5 \times 10^{11}$ cm^{-2}, as both curves follow a very similar line. Reproduced with permission from Ref. [6].

3. Phase diagrams of Moiré superconductors and comparison with HTSc materials

At $\nu \approx -2$, superconductivity was observed in samples M1 and M2 below critical temperatures of up to 3 K. Figures 3a and b present sections of the phase diagram for negative charge carrier densities for the samples M1 ($\Theta = 1.16°$) and M2 ($\Theta = 1.05°$). Here, the $R_{xx}(T)$-curves are plotted as vertical lines indicated by the green dashed line in (b), using color coding for R_{xx}) as function of the charge carrier density. The dashed white lines are defined as 50% resistance to the normal state. Here, we see that the borders of the superconducting domes are not sharp and varying with n, thus leading to a large variation of the superconducting transitions concerning T_c as well as the transition width, δT_c. These diagrams reveal that the twist angle a_M sets the possibility to observe superconductivity, but the resulting superconducting properties of the tBLG samples clearly depend on the charge carrier density.

Preprints.org (www.preprints.org) | NOT PEER-REVIEWED | Posted: 9 June 2023 doi:10.20944/preprints202306.0688.v1

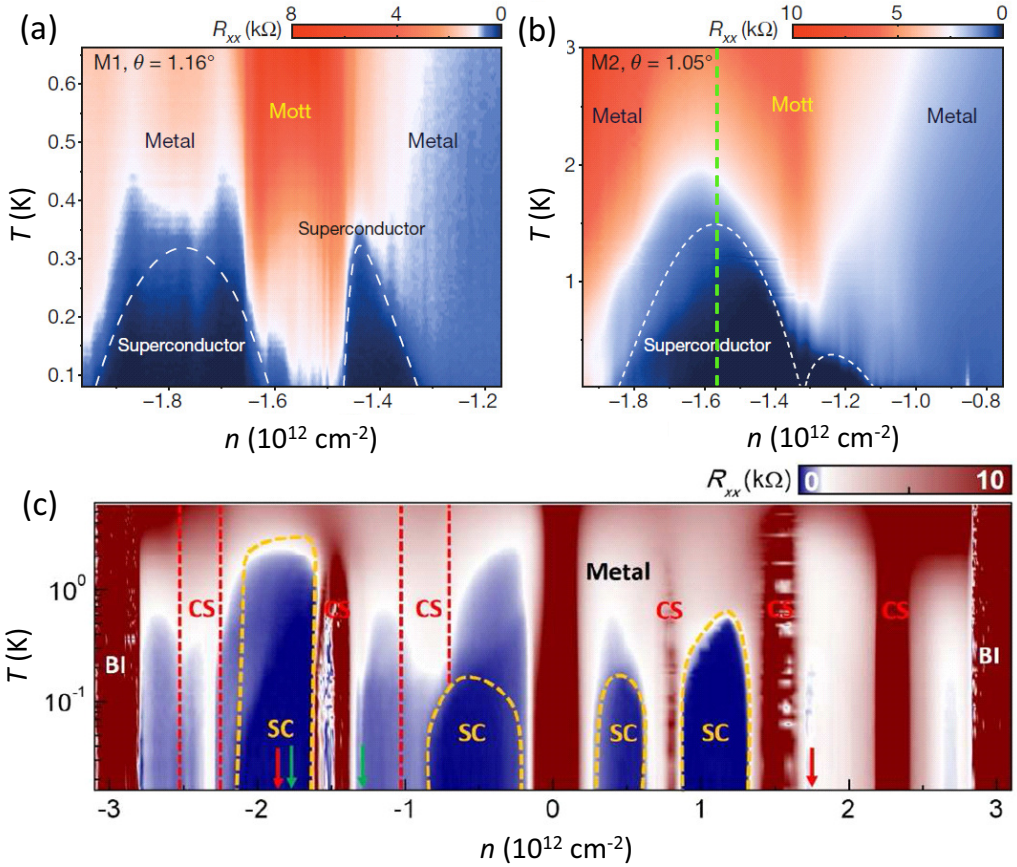

Figure 3. (**a**). Four-probe resistance measurement on sample M1 ($\Theta = 1.16°$). The longitudinal resistance, R_{xx}, is measured at given charge carrier densities versus temperature, i.e., along the dashed-green lines and R_{xx} is represented via the color code, given above the diagram. Two superconducting domes (dark blue/black) are observed next to the half-filling state, which is labelled 'Mott' and centered around $-n_s/2 = -1.58 \times 10^{12}$ cm^{-2}. The remaining regions in the diagram are labelled as 'metal' owing to the metallic-like temperature dependence of R_{xx}. The highest critical temperature observed in device M1 is $T_c = 0.5$ K (at 50% of the normal-state resistance). (**b**), Same measurements as in (**a**), but for device M2, showing two asymmetric and overlapping domes. The highest critical temperature in this device is $T_c = 1.7$ K. (**c**) Colour plot of longitudinal resistance versus charge carrier density and temperature of Ref. [6] on a tBLG sample with $\alpha = 1.1°$ (see also Table 2 below), showing different phases including metal, band insulator (BI), correlated state (CS) and superconducting state (SC). The boundaries of the superconducting domes – indicated by yellow lines – are defined by 50% resistance values relative to the normal state. Note that the transition from the metal to the superconducting state is not sharp at some carrier densities, which renders the proper determination of the value of T_c difficult.

In subseqent papers, a further variation of the charge carrier density revealed a complete sequence of insulating states, magnetic states as well as superconducting states. Such a full phase diagram is shown in Figure 3a, reproduced from Ref. [6] on a tBLG sample with $\alpha = 1.1°$ (see also Table 2 below), presents the complete sequence of superconducting domes (SC), metallic behavior and correlated states (CS) when tuning the gate voltage between $\pm 3 \times 10^{12}$ cm^{-2}. In this diagram, also three new superconducting domes at much lower temperatures were observed, close to the $\nu = 0$ and $\nu = \pm 1$ insulating states. The red and green arrows indicate the superconducting transitions observed by Cao et al. [2] and Yankowitz et al. [3].

The phase diagram of tBLG, plotting temperature vs. charge carrier density is similar to that of the HTSc cuprates (where temperature is plotted vs. the doping level), and includes several dome-shaped regions corresponding to superconductivity. Furthermore, quantum oscillations in the

 doi:10.20944/preprints202306.0688.v1

longitudinal resistance of the material indicate the presence of small Fermi surfaces near the correlated insulating states, which is also the case in underdoped cuprate HTSc. The small Fermi surface of tBLG, corresponding to a charge carrier density of about 10^{11} cm^2, and the relatively high resulting T_c's places the tBLG systems among the superconductors with the strongest pairing strength between electrons [2], which was later relativated by Talantsev [11] based on the thorough analysis of the available magnetic data.

As stated in [2], "one of the key advantages of this system is the in situ electrical tunability of the charge carrier density in a flat band with a bandwidth of the order of 10 meV". This enables the study of the phase diagram to be performed in unprecedented resolution on one given sample, avoiding the problems arising when studying various samples with different microstructures. However, there is also a drawback as the application of the gate voltage does not allow for magnetic measurements in magnetometers to be performed on these devices, so the most important hallmark of superconductivity, the Meissner effect [80,81], cannot be measured directly. For magneto-optic imaging [82,83] or for magnetic force microscopy (MFM) [84], the tBLG devices are too small to enable proper measurements. One could imagine, however, to apply the scanning Hall probes [85,86], scanning SQUID [87] or the diamond color center [88,89] techniques to image the details of the magnetic states in tBLG, which were already predicted in a recent paper [90]. Nevertheless, other features of the superconducting state like the effect of applied magnetic fields on the superconducting transition, and the Fraunhofer patterns could be observed, which enabled a classification of the Moiré superconductors based on the magnetic data as presented by Talantsev [11].

An important experimental work was carried out by Saito et al. [10], demonstrating the effect of varying the thickness of the h-BN layer on the superconducting properties of tBLG, where $d_{\mathrm{h-BN}}$ varies between 6.7 nm and 68 nm for tBLG samples with different twist angles. In this work, the highest observed T_c-values for tBLG samples were reported. Figures 4a–f present the influence of the h-BN cover layer thickness on the superconductivity of the tBLG devices 1 (a) – 5 (e) (Figs. 4a–e reproduced from Saito et al. [10]). The diagrams show the measured, color-coded R_{xx} as function of T and ν. For each device, the values of the twist angle α, its error margin and the thickness d of the h-BN layer are given. The dashed line in each image indicates the density $\nu = -2$. Figure 4f gives a 3D-bar diagram of the highest T_c's recorded as function of d and α. Here, we can see directly that a thicker h-BN layer yields a higher value of T_c (see also the data collected in Table 2 below). The superconducting dome recorded for device 5 at $n = 1.79 \times 10^{12}$ cm^{-2} with $d = 45$ nm and α slightly above the magic angle yielding the highest T_c is the most robust one of sll devices investigated. However, we must note here that the increase of d does not change the charge carrier density in the tBLG. According to Saito et al. [10], the effect of increasing d is due to the separation of the channel from the gates, leading to varying degrees of screening of the Coulomb interaction. Furthermore, other experimentally not controllable parameters like the twist angles between h-BN and tBLG as well as strain may influence the measured T_c. Thus, the error bars shown in Figure 6 below are quite large.

Preprints.org (www.preprints.org) | NOT PEER-REVIEWED | Posted: 9 June 2023 doi:10.20944/preprints202306.0688.v1

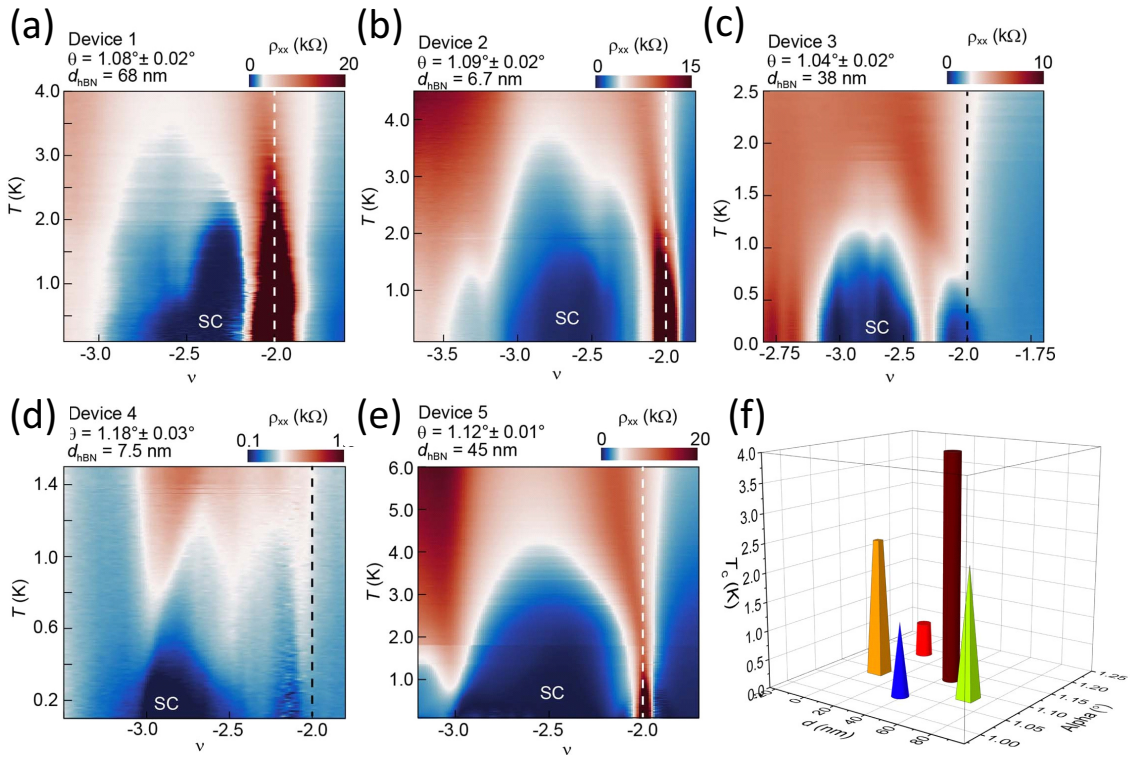

Figure 4. Phase diagrams on tBLG revealing the influence of the h-BN layer thickness. The diagrams are presenting details of the 2D maps around a superconducting dome in each device [10] D1–D5. The white dashed lines show $\nu = -2$. (**a**) Device 1 ($\Theta = 1.08°$, $d_{\mathrm{h-BN}} = 68$ nm, ■). (**b**) Device 2 ($\Theta = 1.09°$, $d_{\mathrm{h-BN}} = 6.7$ nm, ■). (**c**) Device 3 ($\Theta = 1.04°$, $d_{\mathrm{h-BN}} = 38$ nm, ■). The superconducting phase is divided by a weak resistive state around $\nu = -2 - \delta$, which does not match the density of the state at $\nu = -2$, being estimated from the strong resistive states at $\nu = -4, 0, 2, 4$. (**d**) Device 4 ($\Theta = 1.18°$, $d_{\mathrm{h-BN}} = 7.5$ nm, ■). (**e**) Device 5 ($\Theta = 1.12°$, $d_{\mathrm{h-BN}} = 45$ nm, ■). (**f**) 3D-bar diagram showing the highest values of T_c recorded in [10] as function of d and α. It is obvious from images (**a**), (**c**), (**e**) and (**f**) that thicker h-BN layers stabilize a strong and robust superconducting state with the highest T_c value of 3.98 K recorded in (**e**). Reproduced with permission from Ref. [10].

Figures 5a–c show various information on the superconducting state of tBLG (data collected by Lu et al. [6]) when applying an external magnetic field to the tBLG devices. The variation of the longitudinal resistance, $R_{xx}(T)$, is given in Figure 5a for applied magnetic fields of 0, 130, 230 and 300 mT. As expected from a superconducting material, the onset of T_c reduces with the application of a magnetic field until the superconducting transition is completely suppressed in higher fields. Figure 5b gives the resistance, R_{xx} (color-coded), as function of the perpendicularly applied magnetic field, $B_\perp$, and the charge carrier density, n, at a temperature of 16 mK. This diagram directly shows the respective magnetic fields to suppress superconductivity. Finally, Figure 5c shows a Fraunhofer interference pattern measured in the superconducting state, which directly manifests the superconducting character as a measurement of the Meissner effect is not possible for a tBLG device. Figures 5d–f present the analysis of Talantsev et al. concerning the superconduting parameters of tBLG samples. The superconducting parameters were derived from fits to the data of the upper critical field, $H_{c2}(T)$ and the critical current density, $J_c(T)$(self field), following the models by [91–99]. All this gives valuable information on the properties of the superconducting state(s) in tBLG samples.

Preprints.org (www.preprints.org) | NOT PEER-REVIEWED | Posted: 9 June 2023 doi:10.20944/preprints202306.0688.v1

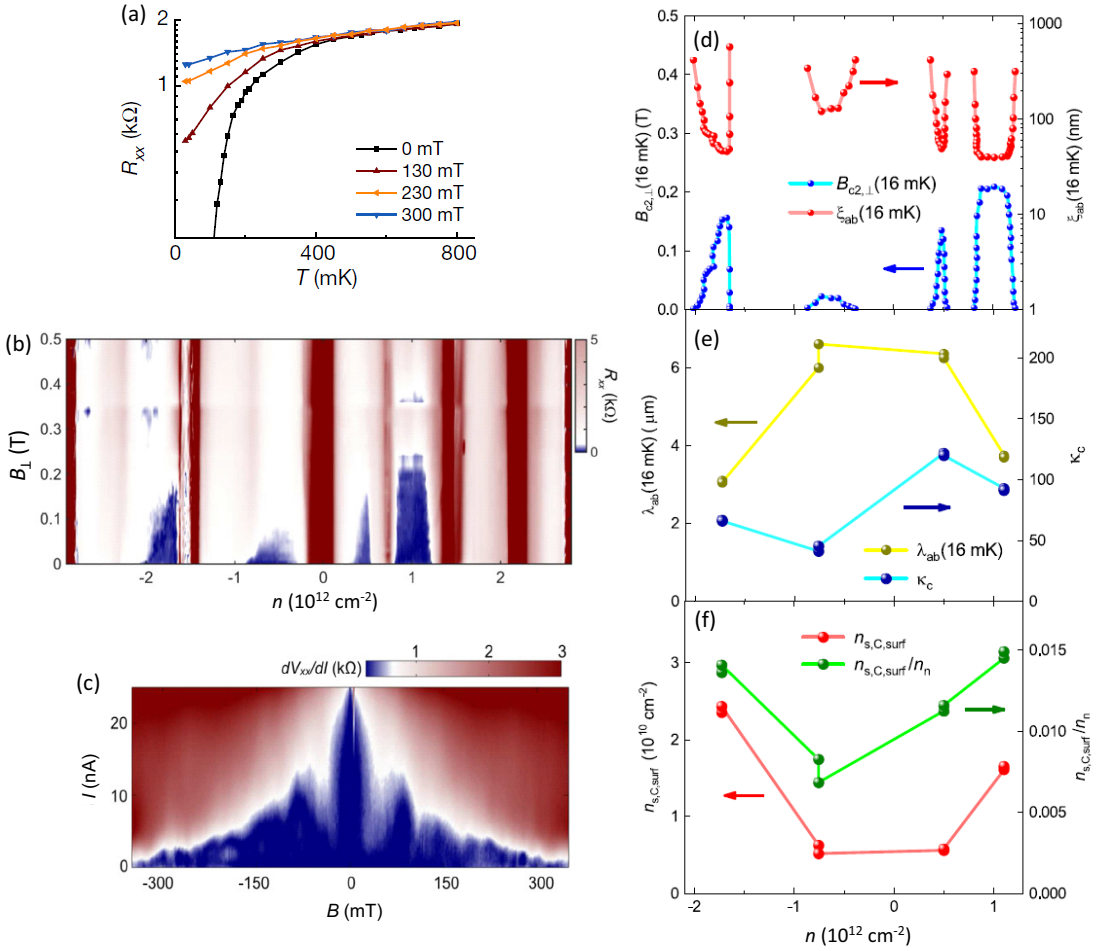

Figure 5. Theeffect of applying external magnetic fields on the superconducting state of tBLG. (**a**) Longitudinal resistance plotted against temperature at various out-of-plane magnetic fields, showing that normal levels of resistance are restored at magnetic fields larger than 300 mT. (**b**) 2D map of longitudinal resistance as a function of B and total charge carrier density n taken at the base temperature 16 mK, demonstrating the effect of perpendicular magnetic field B on the SC pockets observed. (**c**) Fraunhofer interference patterns measured in the superconducting state, charge carrier density 1.11 $\times 10^{12}$ cm^{-2} . Figures a–c: Reproduced with permission from Lu et al. [6]. (**d**) Analysis of the superconducting phase diagram of tBLG with $\Theta \sim 1.1°$. The upper critical field, $B_{c2,\perp}$ (16 mK), and deduced ξ_{ab} (16 mK) using Eq. (1) of Ref. [11]. (**e**) Deduced λ_{ab} (16 mK) and κ_c for four doping states for which I_c(self-field, 16 mK) was reported by Lu et al. (**f**) Cooper pairs surface density, $n_{\mathrm{s,C,surf}}$, and the ratio of $n_{\mathrm{s,C,surf}}/n_n$ for four doping states for which I_c(self-field, 16 mK) was reported by Lu et al. [6]. Figures d–f: taken with permission from Ref. [11].

In Figure 6, the available literature data for $T_{c,\mathrm{opt}}$ are plotted versus the Moiré angle, α. One can see that the highest $T_{c,\mathrm{opt}}$ is obtained at the magic angle of 1.1°, but the area of superconductivity spans the entire region from ∼0.8° to ∼ 1.6°, where $T_{c,\mathrm{opt}}$ is found to be at higher values for $\alpha > 1.1$ as compared to $\alpha < 1.1$. The application of high pressure (1.33 GPa) to the tBLG device as well as the increased size of the h-BN layer was found to lead to higher values of $T_{c,\mathrm{opt}}$.

Preprints.org (www.preprints.org) | NOT PEER-REVIEWED | Posted: 9 June 2023 doi:10.20944/preprints202306.0688.v1

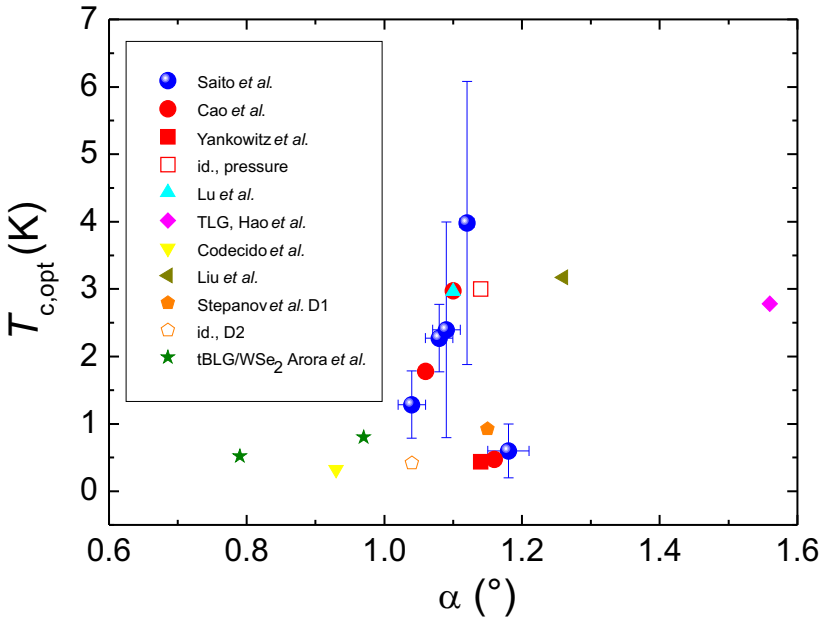

Figure 6. Experimental data for the superconducting transition temperature, $T_{c,\mathrm{opt}}$ (which corresponds to T_c^{MF}) , with the respective error bars. Data were taken from Saito et al. (Ref. [10]), together with data of Cao et al. [2], Yankowitz et al. [3], Lu et al. [6], Liu et al. [8], Codecido et al. [7], Stepanov et al. [9] and Arora et al. [14]. The dahed green line indicates the magic angle, $\Theta_{\mathrm{magic}} = 1.1°$.

Let us here summarize the results being most important for the understanding of superconductivity in the Moiré superconductors.

New results with much higher values of T_c were presented recently by Saito et al. [10], who also used the h-BN as top and bottom cover, but varied the tilt angle between 1.02° and 1.20° and the thickness of the h-BN layer between 6.7 nm and 68 nm. These experiments demonstrated that the device (device 5) with a tilt angle of $\Theta = 1.10$–$1.15°$ and a h-BN thickness of 45 nm showed the highest T_c ever reported for the tBLG systems.

Stepanov et al. [9] also fabricated devices with varying the h-BN thickness between 7 and 12.5 nm.

Codecido et al. [7] demonstrated superconductivity in tBLG at a much smaller angle $\Theta = 0.93°$, so superconductivity does exist in a wide range around the magic angle.

Lu et al. [6] have shown a complete phase diagram of their tBLG sample with four domes of superconductivity at positive and negative charge carrier densities by plotting the measured longitudinal resistance versus temperature and charge carrier density, demonstrating the experimental advances since the first reports of superconductivity in tBLG.

The measurement of a Fraunhofer-like pattern (see Figure 5c) solved the problem of the not observable Meissner effect in the Moiré superconductors and also demonstrated that the charge carriers in tBLG are indeed Cooper pairs. Furthermore, the analysis of the available magnetic data by Talantsev [11] showed that the classical formulae for the self-field critical current density and the upper critical field, $H_{c2}(T)$, can be applied to the tBLG data, which implies that superconductivity of the tBLG is not so unconventional, and the extracted superconducting parameters show that only s-wave and a specific kind of p-wave symmetries are likely to be dominant.

Thus, we list here the most important findings for Moiré superconductors:

- The experiments and analyses indicated that the charge carriers in tBLG are Cooper pairs.
- Superconductivity in the Moiré superconductors shows a reduced level of superconducting charge carriers ($-n_s/2 = \sim 1.58 \times 10^{12}$ cm^{-2}).
- By applying a gate voltage, doping like in a HTSc material can be simulated, and superconducting domes can appear at various values of n_s. As a result, the Fermi temperature, T_F, is completely different from the HTSc as seen in the Uemura plot (see Refs. [2,11] and Figure 7).

 doi:10.20944/preprints202306.0688.v1

- The maximum value of T_c is obtained close to the magic angle of 1.1° (see Figure 6).
- Increasing the thickness of the h-BN layer as done in the experiments of Saito et al. [10] increases the maximum recorded values of T_c, but does not change the superconducting electron density ($\nu = -2.5$).

Here it is important to note that the pairing mechanism leading to the formation of Cooper pairs in Moiré superconductors remains still unknown.

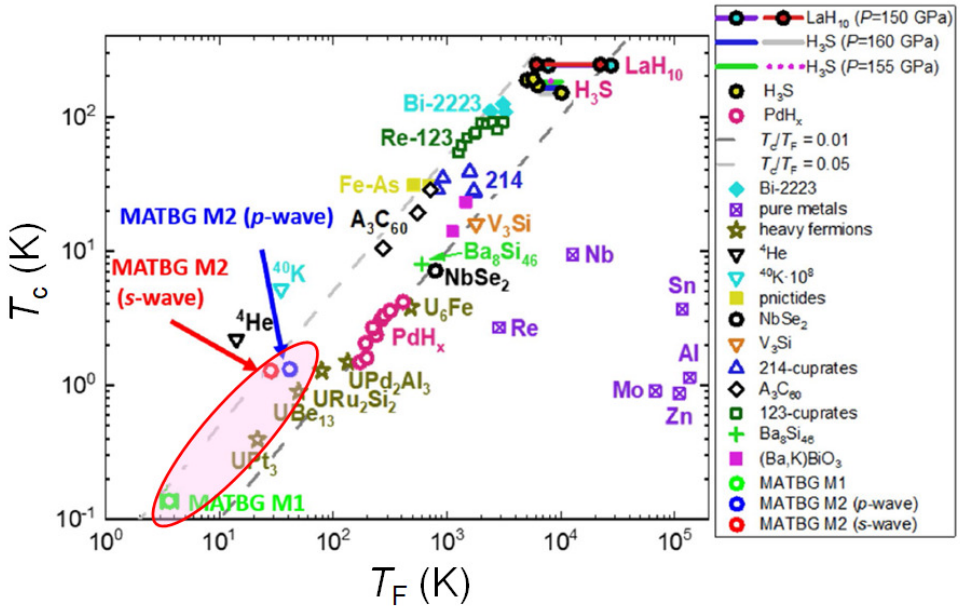

Figure 7. Uemura plot showing the position of tBLG among other most other superconducting materials. Figure reproduced from Talantsev et al. [11].

Now, we can make a comparison of the Moiré superconductors to the HTSc materials, and here especially, the cuprate HTSc. For all the cuprate HTSc, the main element are the Cu-O-planes, which serve as the highway for superconductivity, and the other layers of the crystal structure serve as charge carrier reservoirs or just as spacing layers. Doping can be achieved by means of oxygenation, but also by doping with other atoms, either within the Cu-O-plane or in the charge carrier reservoir layers [100]. The main points are summarized in Table 1.

Table 1. Table showing the differences between HTSc and Moiré superconductors.

	Moiré superconductors	HTSc
layered material	min. 2 layers graphene, WSe_2	Cu-O-planes
superconducting electron density, n_s	1.58×10^{12} cm^{-2}	$\sim 1 \times 10^{14}$ cm^{-2}
superconducting charge carriers	Cooper pairs	Cooper pairs
charge carrier mass	0.2 m_e	
Fermi temperature	$\sim$ 10 K	$\sim$1100 K
tunability of T_c	yes, via gate voltage	yes, via oxygenation or ion doping
Meissner effect	not observable (Fraunhofer pattern)	yes (magnetic measurements)

On the base of all these results collected from the literature, we may now apply the Roeser-Huber formalism to calculate the superconducting transition temperatures of the various Moiré superconductors.

 doi:10.20944/preprints202306.0688.v1

4. Roeser-Huber formalism

The basic idea behind the Roeser-Huber formalism is the view of the resisitive transition to the superconducting state as a resonance effect between the superconducting charge carrier wave (i.e., the Cooper pairs), λ_{cc}, and a characteristic length, $x = \lambda_{cc}/2$, in the sample. Recently, a nice discussion of the critical deBroglie wavelength in superconductors was given by Talantsev [101]. The details of the Roeser-Huber formalism were already discussed previously in Refs. [68,69,74]. To avoid possible misunderstanding, we must point out here that the Roser-Huber formalism is *not* a theory explaining the mechanism of superconductivity, nor does this approach make any use of existing theories like the BCS theory. The goal of the Roser-Huber approach is to establish a relation between superconductivity (carried by Cooper pairs) and a characteristic length in the given crystal structure, which was often demanded in the literature [81], but could not be established using the common theories.

The Roeser-Huber-equation, originally obtained for high-T_c superconductors, is written as

$$\left[(2x)^2 2M_L\right] n_0^{-2/3} \pi k_B T_c = h^2 \quad , \tag{3}$$

where h is the Planck constant, k_B the Boltzmann constant, x the characteristic atomic distance, T_c the superconducting transition temperature, M_L the mass of the charge carriers, and n_0 is a correction factor describing the number of Cu-O-planes in the HTSc unit cell. For $YBa_2Cu_3O_{7-\delta}$ with one Cu-O-plane per unit cell, we have $n_0 = 1$, and the compound $Bi_2Sr_2CaCu_2O_{8+\delta}$ (Bi-2212) with 2 Cu-O-planes per unit cell has $n_0 = 2$. Thus, n for tBLG is taken to be $n = 1$ as the two graphene layers at the magic angle give together one superconducting unit. A system corresponding to $n_0 = 2$ would be then a stack of two 2D layers like h-BN–tBLG–h-BN–tBLG–h-BN, where the two tBLG layers are separated by a h-BN layer. As charge carrier mass, we assume in a first approximation $M_L = 2m_e$, corresponding to a Cooper pair.
An energy, $\Delta_{(0)}$, can be introduced via

$$\Delta_{(0)} = \pi k_B T_c \quad , \tag{4}$$

which may correspond to the pairing energy of the superconductor. So we can write

$$(2x)^2 \cdot 2M_L n_0^{-2/3} \cdot \Delta_{(0)} = h^2 \quad . \tag{5}$$

Using eq. (4) and regrouping of the terms leads finally to

$$\Delta_{(0)} = \frac{h^2}{2} \cdot \frac{1}{M_L} n_0^{2/3} \cdot \frac{1}{(2x)^2} = \pi k_B T_c \quad . \tag{6}$$

It is important to note here that Eq. 6 was reached without the use of any theoretical description of superconductivity, just by the simple quantum mechanics model of a particle in the box [102]. Here, we must note that eq. 3 does not offer many parameters to adapt the formalism described above to the case of tBLG and its derivatives. Thus, only minor adapations can be made: (i) taking $n_0 = 1$ was already mentioned before. (ii) M_L corresponds to the mass of a Cooper pair, so $M_L = 2m_e$. (iii) The Moiré lattice constant, a_M, plays the key role to describe the crystal parameter of a Moiré superconductor, so the characteristic length corresponds to $x = a_M$.

An essential issue to apply the Roeser-Huber formalism is the correct choice for the superconducting transition temperature, T_c. For a proper comparison of the calculated data to the experiments, T_c in the Roeser-Huber formalism is to be taken from resistance measurements as the maximum of the derivative, dR/dT, corresponding to the mean field transition temperature T_c^{MF}, which also plays an important role for the fluctuation conductivity analysis as described in Refs. [103–105]. In the literature, T_c is often derived often from 50% of the normal-state resistance, which is not necessarily the same as T_c^{MF}, especially not in the case of a two-step transition. Both

 doi:10.20944/preprints202306.0688.v1

these definitions of T_c are distinct from the T_c used in the Uemura plot [2,11,106,107], where the completed transition when reaching $R = 0\ \Omega$ is considered. Other authors also have used $T_{(\mathrm{BKT})}$, the Berezinskii–Kosterlitz–Thouless (BKT) temperature, which is well suited for describing the superconducting transition in 2D systems like the ones investigated here. Most of the approaches mentioned here have, however, problems to give a proper value of T_c when the superconducting transition is very broad, shows a secondary step, does not reach $R = 0\ \Omega$ or when the deviation from the normal-state resistivity is difficult to be defined.

Thus, in the present work all the published resistance data of Moiré superconductors were digitalized and the derivative, $\mathrm{d}R/\mathrm{d}T$, was plotted graphically to obtain values for T_c according to the demands of the Roeser-Huber formalism.

5. Application of the Roeser-Huber formalism to Moiré superconductivity

The results discussed in Section 3 provided the base to compare the Roeser-Huber calculations with a wider experimental dataset. For the comparison, we employed the data of Saito et al. (their Figure 3c), and those of Refs. [2,3,6–9,14]. The $T_{c,\mathrm{opt}}$ determined by Saito et al. corresponds directly to T_c^{MF} required by us, so the data can be directly compared to each other as done in Table 2 below. Table 2 presents the T_c-values of several tBLG devices of various authors [2,3,6–10] together with data of a graphene tri-layer [12], the data of WSe_2-stabilized tBLG [14] and the data obtained on twisted WSe_2 bi-layers [15]. Listed are the tilt angle α, the experimentally determined value of $T_c(\mathrm{exp})$ corresponding to our definition of T_c^{MF}, the characteristic length, x, corresponding to the Moiré lattice constant a_{M}, the energy $\Delta_{(0)}$ calculated using $n_0 = 1$, $M_L = 2m_e$ and the calculated values of $T_c(\mathrm{calc})$. When doing the calculations, the calculated values $T_c(\mathrm{calc})$ turned out to be much larger as the experimentally observed values for T_c. The first two rows give the data for tBLG at the magic angle, $\Theta = 1.1°$, yielding 4.23 K with $n_0 = 1$. Using $n_0 = 2$ would lead to a T_c of 6.714 K, which is even higher and unrealistic.

Table 2 shows further that the experimental variation of the tilt angle between 0.93° (the smallest tilt angle reported for superconductivity in tBLG) and 1.18° leads to T_c-values of pure tBLG ranging between 3.024 K and 4.867 K. Thus, all calculated data are clearly higher than the experimental ones. What could be the reason for this?

There are two possible scenarios to explain this outcome.

(1) The effective Moiré lattice parameter in the final devices is much larger as determined by eq. (1).

This situation is possible when considering the fact that Moiré superlattices can be formed by all layers involved forming the device, not only the graphene bilayer as intended. This was also mentioned as possible source for errors by Saito et al. [10] when varying the h-BN thickness. The fully encapsulated graphene has necessarily two interfaces with the h-BN layers on the top and bottom, where an extra tilt can occur. Looking at Figure 1c and eq. (1), the effect is largest at very small angles.Thus, attempting to align the top and bottom h-BN layer to the graphene may generate much larger Moiré superlattice parameters. Such a situation was discussed by Wang et al. [51].
In case of a stack of h-BN with graphene, there is a misfit between the two lattices, so the resulting superlattice can be described as [3,53]

$$a_{\mathrm{MSL}} = \frac{(1+\delta)a_0}{\sqrt{2(1+\delta)(1-\cos\Phi)+\delta^2}} \quad , \tag{7}$$

where δ denotes the lattice mismatch between h-BN and graphene (1.8 %) and Φ is the twist angle of h-BN with respect to graphene. A result of this is that the largest possible Moiré lattice constant is $\sim$ 14 nm, which occurs when the one graphene layer is fully aligned to the h-BN layer. Wang et al. showed that they can increase the MSL lattice parameter to 29.6 nm by aligning both h-BN layers to the graphene. Calculating T_c with this MSL parameter would yield a value of $\sim$0.8 K, which would be much closer to the experimental data.

 doi:10.20944/preprints202306.0688.v1

Table 2. Table giving the experimental data of T_c, the angles and the resulting characteristic length, x, the calculated energy $\Delta_{(0)}$ and $T_c(\mathrm{calc})$ using the Roeser-Huber equation (eq. 3 with n =1 and $M_L = 2m_e$. The energy $\Delta^*_{(0)}$ and the transition temperature $T^*_c(\mathrm{calc})$ are calculated using the correction factor η. Furthermore, the sample names of the original publication and the references are given. The T_c marked by † is the value claimed by the authors from a two-step transition. Our T_c determined from their data is $T_c = 0.32$ K. ‡ This value gives the zero resistance. Stars (*) mark the WSe_2 T_c-data from the experiments of An et al. [15], where the T_c values given are determined by us. ($^{\otimes}$) as given by the authors for $R = 0\ \Omega$. (**) indicates T_c determined via a 50% normal-state resistance criterion.

type	tilt angle α [°]	$T_c(\mathrm{exp})$ [K]	x [nm]	$\Delta_{(0)}$ [10^{-22} J]	$T_c(\mathrm{calc})$ [K]	$\Delta^*_{(0)}$ [10^{-22} J]	$T^*_c(\mathrm{calc})$ [K]	η	**comment/ sample name**	**Ref.**
tBLG	1.1	–	12.81	1.835	4.23	—	—	—	$n_0 = 1$	magic angle
	1.1	–	12.81	2.912	6.714	—	—	—	$n_0 = 2$	
tBLG	1.16	0.47	12.15	2.040	4.704	0.204	0.470	20	M1	Cao et al. [1,2]
	1.05	1.7	13.42	1.671	3.854	0.740	1.705	4.52	M2	Cao et al. [1,2]
	1.14	0.6	12.36	1.971	4.542	0.197	0.454	20	D1	Yankowitz et al. [3]
	1.27	3	11.10	2.446	5.638	1.304	3.007	3.75	D2 (1.33 GPa)	Yankowitz et al. [3]
	1.08	2.27	13.05	1.768	4.877	0.982	2.265	3.6	device 1	Saito et al. [10]
	1.09	2.395	12.93	1.801	4.153	1.044	2.408	3.45	device 2	Saito et al. [10]
	1.04	1.29	13.55	1.639	3.781	0.561	1.295	5.84	device 3	Saito et al. [10]
	1.12	3.98	12.58	1.902	4.385	2.606	3.986	2.2	device 5	Saito et al. [10]
	1.18	0.6	11.94	2.111	4.867	1.792	0.601	16.2	device 4	Saito et al.[10]
	1.1	0.25	12.81	1.835	4.23	1.287	2.968	2.85	–	Lu et al. [6]
	0.93	<0.5 †	15.16	1.311	3.024	0.139	0.32	18.9	smallest Θ	Codecido et al. [7]
	1.26	<3.5 ‡	11.19	2.407	5.550	1.376	3.171	3.5	–	Liu et al. [8]
	1.15	0.92	12.26	2.005	4.632	0.401	0.925	10	D1	Stepanov et al. [9]
	1.04	0.4	13.55	1.640	3.781	0.786	0.398	19	D2	Stepanov et al. [9]
TLG	1.56	2.7	9.035	3.69	8.507	1.19	2.784	6.2	–	Hao et al. [12]
tBLG+	0.97	0.8	14.53	1.43	3.289	0.348	0.802	8.2	D1	Arora et al. [14]
WSe_2	0.79	0.52	12.73	0.946	2.182	0.225	0.520	8.4	D3	
bi-layer	1	3.32*	18.89	0.844	1.95 ($n_0 = 1$)	—	—	—	E7, -14.4 V	An et al. [15]
WSe_2	1	$3^{\otimes}$	18.89	1.340	3.09 ($n_0 = 2$)	—	—	—	–,–	
	1	$3^{\otimes}$	20	0.753	1.74 ($n_0 = 1$)	—	—	—	–,–	
	1	$3^{\otimes}$	20	1.195	2.76 ($n_0 = 2$)	—	—	—	–,–	
	2	4.53*	9.45	3.376	7.78 ($n_0 = 1$)	1.963	4.53	3.44	F2, -6.65 V	
	2	6.1*	9.45	3.376	7.78 ($n_0 = 1$)	2.648	6.11	2.55	F2, -6.92 V	
	4	6 (50%)**	4.72	13.5	31.1 ($n_0 = 1$)	—	—	—	D11, -17.9 V	

 doi:10.20944/preprints202306.0688.v1

However, the high pressure experiment of Yankowitz et al. [3] and the data of Saito et al. [10] demonstrated that this explanation cannot be the solution of the present problem. The optical images of the devices presented by Cao et al. [2], Yankowitz et al. [3] and Saito et al. [10] showed all arrangements made before putting the top h-BN layer in place. Thus, the misfit would be created when placing this layer. While this scenario might have applied to the first reports of superconducting tBLG, all authors of the more recent contributions have explicitly checked for such effects and even provided a dedicated discussion in their Supplementary Data (see, e.g., Figure S2 of Ref. [6]), so this effect can be ruled out as the main reason. Furthermore, the high-pressure experiment could increase T_c from 0.6 K to 3 K with the same configuration, and the data of Saito et al. [10] showed that their experimental values of T_c are approaching the calculated ones using $M_L = 2m_e$.

(2) The choice of $M_L = 2m_e$ does not properly describe the Moiré superconductors. As seen from the Uemura plot of Figure 7, the Fermi temperature, T_F, which includes both the effective mass of the charge carriers as well as the charge carrier density, is located for tBLG in a completely different position as the HTSc or metallic superconductors.

Equation (3) does not contain a parameter accounting for the small charge carrier density in the tBLG materials, nor is there a possibility to choose the right charge carrier density for a specific superconducting dome. However, the parameter n_0 (which was set = 1 for the tBLG) was derived in Ref. [68,69] by comparing the lowest level energy of the PiB approach, i.e., $E_1 = \frac{h^2}{8M_L x^2}$ with the Fermi energy, $E_F = \frac{h^2}{8M_{\text{eff}}} N_c^{2/3} \left[\frac{3}{\pi}\right]^{2/3}$. If the carrier density increases by a factor n, the Fermi energy increases by $E_F \sim (nN_c)^{2/3} = n^{2/3}(N_c)^{2/3}$. The parameter n_0 was then deduced as an integer number describing the number of the Cu-O planes. Having a material with two Cu-O planes, the number of charge carriers doubles. Thus, a similar approach could be made to account for the changes of the charge carrier density in the case of the tBLG superconductors. As band structure calculations revealed a small mass of the charge carriers in tBLG [2], this change of the charge carrier mass could be implemented in the mass, M_L.

A very important point is further that the Roeser-Huber formalism allows another test of the calculated data, the so-called Roeser-Huber plot [68,69,74]. It was found that all the superconducting materials investigated up to now (HTSc, metallic superconductors) fall on a common correlation line with a slope $h^2/(2\pi k_B) = 5.061 \times 10^{-45}$ m^2 kg K. This line is drawn as dashed red line (- - - - -) in Figure 8. The black squares (■) correspond to the data obtained for various metals and HTSc as published in Ref. [74]. The linear fit to these data (dashed-blue line, - - - - -) is almost perfect (i.e., close to the dashed red line) with only a small error margin, which manifests the basic idea of the Roeser-Huber formalism.

Now, we plot the calculated T_c values for the tBLG samples in the same graph using half-filled symbols. The basic data for various Moiré lattic parameters, $a_M = 0.7°$, 1.1° and 1.3°, are shown by the violet circles. The light green up-triangles give the calculated T_c for the devices D1, D2 (Yankowitz) and device 5 (Saito). When plotting these data versus the experimentally determined T_c's, we obtain the dark green left triangles. We see that all these values lie on a nearly straight line which crosses the correlation line indicating a clear misfit of the parameters entering the calculation.

Thus, the introduction of a new correction factor is fully justified as the band structure calculations have shown that the charge carrier density of the tBLG at the magic angle is very small, and it is shown by Lu et al. [6] that several superconducting domes can be found when plotting the linear resistance versus carrier density and temperature (see Figure 3), which equals a phase diagram of tBLG. Thus, this fact must be accounted for in the Roeser-Huber formalism. Cao et al. [2] showed that the effective mass of the charge carriers is only 0.2 m_e, and in the Uemura plot [106,107] (their Figure 6 and our Figure 7), they demonstrated that the tBLG samples are located at *low* Fermi temperatures $T_F \approx 20$ K and $n_{2D} = 1.5 \times 10^{11}$ cm^{-2}, being clearly distinct from the HTSc (see Table 1), where the choice $M_L = 2m_e$ applies very well.

Preprints.org (www.preprints.org) | NOT PEER-REVIEWED | Posted: 9 June 2023 doi:10.20944/preprints202306.0688.v1

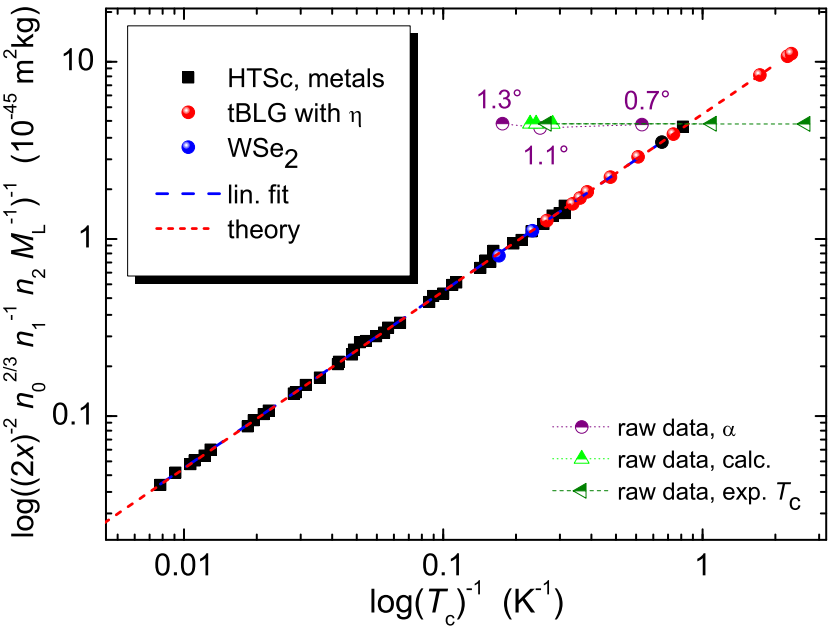

Figure 8. Roeser-Huber plot including the data of the various tBLG samples (●) and WSe_2 (●) and the previously calculated data for several HTSc and metals/alloys (■). The straight red-dotted line follows the equation for a particle in a box [102] and the blue dashed line gives the linear fit to the data (see text).

Now, it is the question how this new correction factor should look alike. To get an idea of the required values, we may use the experimentally available data for T_c and plot these data versus the required correction factor, η. The result of this procedure is shown in Figure 9. The dashed green line indicates the bottom value of $\eta = 2$, which corresponds to the case of HTSc materials. The lower the measured transition temperature, the larger the parameter η. Fitting the data with an exponential decay of the type

$$y = 2A_1 \cdot \exp((x - x_0)/t_1) \quad , \tag{8}$$

we obtain a quite good correlation with the parameters $A_1 = 14.17$, $x_0 = 0.6$ and $t_1 = 0.766$ as shown in Figure 9. The tBLG/WSe_2-data fall below this fit line, and the TLG and WSe_2 are located above it. Furthermore, the values for η are only in a small range between 2 and 22, which is equal to the narrow window for the tBLG samples in the Uemura plot (T_c as a function of the Fermi temperature, $T_F = E_F/k_B$ with E_F denoting the Fermi energy) in a line below the HTSc samples [2,11]. As T_F is directly linked to the Fermi velocity, v_F, via

$$T_F = \frac{m^* v_F^2}{2k_B} \tag{9}$$

and

$$v_F = \frac{h}{2\pi m_e}(2\pi^2 n)^{1/3} \quad , \tag{10}$$

there is the effective mass, m^*, and the density of the charge carriers, n, directly involved. Thus, the parameter η determined here should contain all this information, which will then also enable to judge via the value of m^* the relation $m^* < 0.1m_e$, if a material can be a superconductor or not [11]. Thus, this parameter η is by no means an artificial approach just to obtain the right T_c-values, but the parameter contains all the essential physics (charge carrier density, charge carrier mass) to describe a given superconducting material. So, the parameter η will further contribute to reduce the calculation error(s) in the Roeser-Huber formalism existing for some other materials like the superconducting elements Nb or Re (see their position in the Uemura plot given in Figure 7), and also solve the long-standing

Preprints.org (www.preprints.org) | NOT PEER-REVIEWED | Posted: 9 June 2023 doi:10.20944/preprints202306.0688.v1

problem of the choice of the proton mass for M_L (the Fermi temperature for metals is ranging between 10^4 K and 1.2×10^5 K, which is 10 to 100 times higher as for the HTSc).

Thus, we introduce a correction factor, named η, to the charge carrier mass M_L in eq. (3) by writing:

$$M_L = \eta m_e \quad . \tag{11}$$

The situation $\eta = 2$ will then correspond to our initial value of 2. Now, we come back to Table 2. The energy $\Delta^*_{(0)}$ and the corresponding $T_c^*(\text{calc})$ were obtained by introducing the correction factor η to the Roeser-Huber equation, which is listed as well. The parameter η was obtained by adapting the calculation procedure manually to the experimentally obtained values of T_c. The result of this procedure is that we can now fully reproduce all the experimentally observed values for T_c. The slight deviations in $T_c(\text{calc})$ account for the difficulties when extracting the T_c-values. The data for the h-BN–WSe_2–tBLG–h-BN stacks of Arora et al. [14] show that the WSe_2-layer stabilizes superconductivity at angles much smaller than the magic angle, and also smaller (0.79°) as the smallest angle reported for pure tBLG. We further note that such a monolayer of WSe_2 is not superconducting on its own; Arora et al. describe the WSe_2-layer in the their paper as insulating [14]. The trilayer graphene (TLG, Hao et al. [12]) would have a quite high T_c of 8.5 K when calculating with $M_L = 2$ due to the small value of a_M. Thus, the required η is quite large and also off the fit in Figure 9.

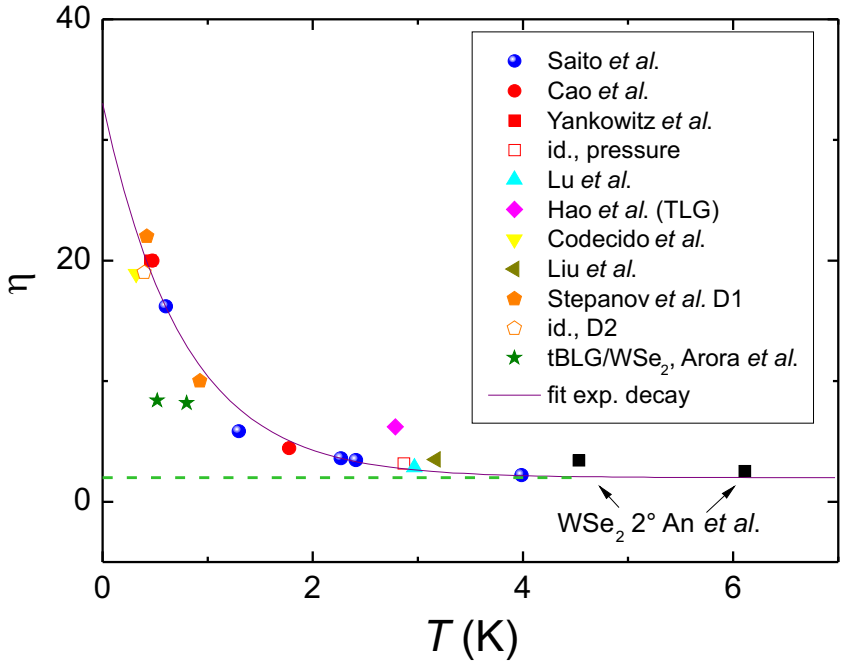

Figure 9. The correction factor η as function of temperature. Included here are the tBLG data of Refs. [2,3,6–10], the trilayer graphene (TLG) of Hao et al. (♦, [12]), the tBLG/WSe_2 of Arora et al. (★, [14]) and the 2° WSe_2 data of An et al. (■, [15]). The violet line (—) is a fit to all data using eq. (8).

The case of bi-layer WSe_2 [15] is more complicated to be solved. The first problem in the case of WSe_2 is the value for n_0 to be taken in the calculations. If a monolayer WSe_2 is superconducting itself, n_0 must be taken as 2. If only the product from two misaligned WSe_2 layers is superconducting, we would have $n_0 = 1$ like for tBLG. A first glance on Table 1 gives the idea that $n_0 = 2$ could be correct, but as seen from the combined WSe_2–tBLG-data from Arora et al. [14], we can consider $n_0 = 1$ to be the more realistic case. Thus, we have listed both cases in Table 1 to give some predictions of T_c for the WSe_2 system. As seen from Figure 1c, the larger lattice parameter of WSe_2 will lead to slightly larger a_M for a given angle Θ, and thus, the resulting values for T_c are higher as compared to tBLG, which is also observed experimentally [15]. The main problem is now that the experiments of Ref. [15] do not convincingly demonstrate superconductivity in this system as compared to the tBLG data, where much

 doi:10.20944/preprints202306.0688.v1

more detailed information is available. So it is difficult to extract properly defined values for T_c from the data presented (WSe_2 bilayers with 1°, 2 ° and 4° misalignment). For the 1° sample (E7), T_c could be around 3.5–4 K, for the 2° sample (F^2) ∼4 K (-6.65 V) or ∼6 K (-6.92 V) and for the 4° sample (D11, marked by a star in Table 1), one may get T_c somewhere between 4 K and 12 K, if at all. The calculation of the Moiré pattern parameter for the 4° sample gives $a_M = 4.72$ nm, which would yield a T_c of 49.9 K (with $n_0 = 2$) or 31.13 K with $n_0 = 1$. These values for $\Delta_{(0)}$ and T_c are considerably too high and unrealistic. As the authors show in their paper higher order Laue reflexes from electron diffraction patterns for the 1° sample, which would indicate a lattice constant of the order of 20–25 nm (instead of the calculated 18.9^circ using eq. (1)), we have used 20 nm for x in Table 2 for the 1° sample and left the 4° sample out of further consideration. If we calculate T_c using $n_0 = 2$, the calculated values come quite close to the experimental data assuming $T_c \sim 3$ K. In all cases, the superconductivity is best documented for sample F^2 (their Figs. 5a and S11), yielding a T_c of 4.53 K (-6.65 V) and 6.1 (-6.92 V) at two different gate voltages. These T_c-values are clearly higher than those of tBLG, but also smaller than the calculated value of 7.78 K ($n_0 = 1$). Determining the correction factors η for this sample yields $\eta = 3.44$ and 2.55 at the two gate voltages, which are only small corrections. To summarize this part, the published data of WSe_2 are not suitable for a good comparison, but when extracting T_c via the first derivative from the published data (best for sample F^2), we only require small correction factors to reproduce the experimental T_c. This would indicate that the WSe_2 bilayers have properties being more similar to that of HTSc compounds.

Coming now back to the Roeser-Huber plot of Figure 8, the red data points (•) give the final results with the correction factor η for the various tBLG samples investigated in the literature (Table 2), and the blue bullet (•) shows the data of the 2° WSe_2 sample.

A more dedicated analysis of all the data available (tBLG samples as well as the extreme elemental superconductors like Bi or Li) will allow to further clarify the properties of η. Here, we can state that η is directly proportial to the effective charge carrier mass, m^*, and the charge carrier density enters the formula like the parameter n_0. For this, we may define a relation $n_d = n_s(\text{tBLG})/n_s(\text{HTSc})$. In this way, the different value of n_s appears as a percentage of the HTSc value, like $n_d = 0.00158$, and in the final formula as $n_d^{2/3} = 0.0136$.

Harshman and Fiory [108] presented another way of calculating the transition temperature of tBLG from experimental data. Also this approach was originally developed for HTSc samples, and the parameters involved are quite similar to those of the Roeser-Huber approach. However, there is no relation between the T_c and the crystal lattice parameters, except a distance between the superconducting layers, which in turn is not contained in the Roeser-Huber formalism. In all cases, it will be interesting to compare the various parameters of the models with each other.

So, we can say here that an extension of the Roeser-Huber formula is required to account for the low charge carrier densities of the tBLG materials and the resulting low charge carrier mass using the new parameter η. When doing so, we can directly reproduce the experimental data of the various tBLG measurements published in the literature, and the resulting data fit very well to the correlation line of the Roeser-Huber plot (see Figure 8).

We further must note here that the calculation performed using $\eta = 2$, that is, a charge carrier mass of $2m_e$, yields an upper limit for T_c of Moiré superconductors, to which the experiments come now close by applying pressure or using thicker h-BN layers (see, e.g., the results of Yankowitz [3] and Saito et al. [10]). Thus, using the Roeser-Huber formalism *without* the specific knowledge of effective charge carrier mass and charge carrier density, provides in turn an upper limit for T_c. This observation is a very positive output for use of the Roeser-Huber equation to predict the superconducting transition temperatures of still unknown materials without the knowledge of n_s or m^*.

6. Conclusions and outlook

As outlook for future research in the field of Moiré superconductivity, one can state that the Moiré superlattices have developed into excellent platforms for the study of new properties of layered

 doi:10.20944/preprints202306.0688.v1

2D materials in general [109], where superconductivity is only one of several special properties. The recent creation of devices with 3, 4 or more graphene layers demonstrated stable and robust superconductivity, and the finding of the dependence of T_c on the h-BN layer thickness also clearly showed that more robust superconductivity is possible in the Moiré superconductors. Thus, one may expect creation of new superconducting materials by different types of stacking the layers, e.g., the combination of graphene and WSe_2, combinations with flat 2D-layers like borophene, stannene [17,18], etc., or even heuslerenes [110], which may be superconducting themselves or not. In all cases, the reviewed research is only the top of an iceberg, as countless other combinations are theoretically possible. Another interesting aspect is the finding of Moiré pattern on the surface of a topological insulator [111,112], combining two ongoing research directions. Also here, more stable and robust new superconducting states may result, which will further widen up the knowledge of such unconventional superconductors.

To summarize up the present paper, in the first part we have given a summary of the various measurements on superconducting tBLG samples as published in the literature. For the measurements, a typical structure called device was build up consisting of the tBLG, a top and bottom h-BN layer and graphite as a substrate and cover for better handling of the structure. Via electric contacts, the longitudinal resistance, R_{xx}, could be measured as function of temperature, applied magnetic field, tilt angle, and h-BN layer thickness. An important result is here that the complete phase diagram (in analogy to the phase diagram of HTSc) could be measured by electrically tuning the charge carrier density, n. This enables a complete study of the superconducting properties of the various tBLG samples for a given tilt angle of the graphene layers. Furthermore, measuring the characteristic Fraunhofer patterns enables a direct proof of the superconducting state, which is important as the classical Meissner effect can not be magnetically measured in these tBLG devices.

All the data of the superconducting state collected by various authors now enable the calculation of T_c of Moiré superconductors based on the Moiré lattice parameter using the Roeser-Huber formalism. When doing so, we find that the Roeser-Huber formula in the standard form with $M_L = 2\, m_e$ yields an upper limit of T_c for tBLG, which is close to the experimental observations for tBLG samples under pressure or with thicker h-BN layers. To better describe the superconducting state(s) of the various tBLG samples and to account for the distinctly different Fermi temperatures, the introduction of a correction factor η to the Roeser-Huber formalism enables to account for the small charge carrier densities and charge carrier mass, so that the experimentally obtained data can successfully be reproduced. All the calculated data with well to the correlation line in the Roeser-Huber plot. Further work is required to find a theoretical foundation for the new parameter η, but it is already obvious that the Fermi temperature, T_F, containing the charge carrier density n_s and the effective charge carrier mass plays an important role. Via T_F and the corresponding Fermi velocity, v_F, it becomes even possible to introduce a criterion to the Roeser-Huber formalism to distinguish if a given material can be a superconductor or not. For the tilted superconducting WSe_2 layers, which were already discussed in the literature, the currently available experimental data are not sufficient to extract proper values for T_c to enable a comparison with the calculated data.

Author Contributions: Conceptualization, M.R.K.; Formal Analysis, A.K.-V. and M.R.K.; Investigation, A.K.-V. and M.R.K.; Writing-Original Draft Preparation, M.R.K.; Writing-Review and Editing, A.K.-V. and M.R.K.

Funding: This work is part of the SUPERFOAM international project funded by ANR and DFG under the references ANR-17-CE05-0030 and DFG-ANR Ko2323-10, respectively.

Institutional Review Board Statement: not applicable.

Informed Consent Statement: not applicable.

Data Availability Statement: Datasets obtained and analyzed during the study are available from the corresponding author on reasonable request.

Conflicts of Interest: The authors declare no conflict of interest.

 doi:10.20944/preprints202306.0688.v1

References

1. Yuan Cao, Y.; Fatemi, V.; Demir, A.; Fang, S.; Tomarken, S.L.; Luo, J.Y.; Sanchez-Yamagishi, J.D.; Watanabe, K.; Taniguchi, T.; Kaxiras, E.; Ashoori, R.C.; Jarillo-Herrero, P. Correlated insulator behaviour at half-filling in magic-angle graphene superlattices. *Nature* **2018**, *55*, 80-84; doi: doi:10.1038/nature26154.
2. Cao, Y.; Fatemi, V.; Fang, S.; Watanabe, K.; Taniguchi, T.; Kaxiras, E.; Jarillo-Herrero, P. Unconventional superconductivity in magic-angle graphene superlattices. *Nature* **2018** *556*, 43–50; doi:10.1038/nature26160.
3. Yankowitz, M.; Chen, S.; Polshyn, H.; Zhang, Y.; Watanabe, K.; Taniguchi, T.; Graf, D.; Young, A. F.; Dean, C. R. Tuning superconductivity in twisted bilayer graphene. *Science* **2019** *363*, 1059–1064; doi: 10.1126/science.aav1910.
4. Suárez Morell, E., Correa, J. D., Vargas, P., Pacheco, M.; Barticevic, Z. Flat bands in slightly twisted bilayer graphene: tight-binding calculations. Phys. Rev. B 82, 121407 (2010).
5. G. Trambly de Laissardière, D. Mayou, and L. Magaud Localization of Dirac Electrons in Rotated Graphene Bilayers. *Nano Lett.* **2010**, *10*, 804–808; doi: 10.1021/nl902948m.
6. Lu, X.; Stepanov, P.; Yang, W.; Xie, M.; Ali Aamir, M.; Das, I.; Urgell, C.; Watanabe, K.; Taniguchi, T.; Zhang, G.; Bachtold, A.; MacDonald, A. H.; Efetov, D. K. Superconductors, orbital magnets and correlated states in magic-angle bilayer graphene. *Nature* **2019** *574*, 653–657; doi: 10.1038/s41586-019-1695-0.
7. Codecido, E.; Wang, Q.; Koester, R.; Che, S.; Tian, H.; Lv, R.; Tran, S.; Watanabe, K.; Taniguchi, T.; Zhang, F.; Bockrath, M.; Lau, C. N. Correlated insulating and superconducting states in twisted bilayer graphene below the magic angle. *Sci. Adv.* **2019** *5*, eaaw9770; doi: 10.1126/sciadv.aaw9770.
8. Liu, X.; Hao, Z.; Khalaf, E.; Lee, J.-Y.; Watanabe, K.; Taniguchi, T.; Vishwanath, A.; Kim, P. Tunable spin-polarized correlated states in twisted double bilayer graphene. *Nature* **2020** *583*, 221–225; doi:10.1038/s41586-020-2458-7.
9. Stepanov, P.; Das, I.; Lu, X.; Fahimniya, A.; Watanabe, K.; Taniguchi, T.; Koppens, F. H. L.; Lischner, J.; Levitov, L.; Efetov, F. K. Untying the insulating and superconducting orders in magic-angle graphene. *Nature* **2020** *583*, 375–378; doi: 10.1038/s41586-020-2459-6.
10. Saito, Y.; Ge, J.; Watanabe, K.; Taniguchi, T.; Young, A. F. Independent superconductors and correlated insulators in twisted bilayer graphene *Nature Phys.* **2020** *16*, 926–930; doi: 10.1038/s41567-020-0928-3.
11. E. F. Talantsev, E.. F.; Mataira, R. C.; Crump, W. P. Classifying superconductivity in Moiré graphene superlattices. *Sci. Rep.* **2020** *10*, 212; doi: 10.1038/s41598-019-57055-w.
12. Hao, Z.; Zimmerman, A. M.; Ledwith, P.; Khalaf, E.; Najafabadi, D. H.; Watanabe, K.; Taniguchi, T.; Vishwanath, A.; Kim, P. Electric field–tunable superconductivity in alternating-twist magic-angle trilayer graphene. *Science* **2021** *371*, 1133–1138; doi: 10.1126/science.abg0399.
13. Guorui Chen, C.; Sharpe, A.L.; Gallagher, P.; Rosen, I.T.; Fox, E.J.; Jiang, L.; Lyu, B.; Li, H.; Watanabe, K.; Taniguchi, T.; Jung, J.; Shi, Z.; Goldhaber-Gordon, D.; Zhang, Y.; Wang, F. Signatures of tunable superconductivity in a trilayer graphene moiré superlattice. Nature 572, 215–219 (2019). https://doi.org/10.1038/s41586-019-1393-y.
14. Arora, H. S.; Polski, R.; Zhang, Y.; Thomson, A.; Choi, Y.; Kim, H.; Lin, Z.; Wilson, I. Z.; Xu, X.; Chu, J.-H.; Watanabe, K.; Taniguchi, T.; Alicea, J.; Nadj-Perge, S. Superconductivity in metallic twisted bilayer graphene stabilized by WSe_2. *Nature* **2020** *583*, 379-384; doi: 10.1038/s41586-020-2473-8.
15. An, L.; Cai, X.; Pei, D.; Huang, M.; Wu, Z.; Zhou, Z.; Lin, J.; Ying, Z.; Ye, Z.; Feng, X.; Gao, R.; Cacho, C.; Watson, M.; Chen, Y.; and Wang, N. Interaction effects and superconductivity signatures in twisted double-bilayer WSe_2. *Nanoscale Horiz.* **2020** *5*, 1309; doi: 10.1039/d0nh00248h.
16. Balents, L.; Dean, C. R.; Efetov, D. K.; Young, A. F. Superconductivity and strong correlations in moiré flat bands. *Nature Phys.* **2020** *16*, 725–733; doi: 10.1038/s41567-020-0906-9.
17. Liao, M.; Zang, Y.; Guan, Z.; Li, H.; Gong, Y.; Zhu, K.; Hu, X.-P.; Zhang, D.; Xu, Y.; Wang, Y.-Y.; He, K.; Ma, X.-C.; Zhang, S.-C.; Xue, Q.-K. Superconductivity in few-layer stanene. *Nature Phys.* **2018**, *14*, 344–348; doi: 10.1038/s41567-017-0031-6.
18. Yan, L.; Liu, P.-F.; Li, H.; Tang, Y.; He, J.; Huang, X.; Wang, B.-T.; Zhou, L. Theoretical dissection of superconductivity in two-dimensional honeycomb borophene oxide B_2O crystal with a high stability. *npj Computational Materials* **2020**, *6*, 94; doi: 10.1038/s41524-020-00365-9.
19. Bistritzer, R.; MacDonald, A. H. Moiré bands in twisted double-layer graphene. *Proc. Natl. Acad. Sci.* **2011** *108*, 12233–12237; doi: 10.1073/pnas.1108174108.

20. Wu, F.; Hwang, E.; Das Sarma, S. Phonon-induced giant linear-in-T resistivity in magic angle twisted bilayer graphene: Ordinary strangeness and exotic superconductivity. *Phys. Rev. B* **2019** *99*, 165112; doi: 10.1103/PhysRevB.99.165112.
21. Schrade, C.; Fu, L. Spin-valley density wave in moiré materials. *Phys. Rev. B* **2019** *100*, 035413; doi: 10.1103/PhysRevB.100.035413.
22. Carr, S., Fang, S., Po, H. C., Vishwanath, A. Kaxiras, E. Derivation of Wannier orbitals and minimal-basis tight-binding Hamiltonians for twisted bilayer graphene: first-principles approach. Phys. Rev. Res. 1, 033072 (2019).
23. Lian, B., Wang, Z. Bernevig, B. A. Twisted bilayer graphene: a phonon-driven superconductor. Phys. Rev. Lett. 122, 257002 (2019).
24. Shi, L.; Ma, J., Song, J. C. W. Gate-tunable flat bands in van der Waals patterned dielectric superlattices. *2D Mater.* **2020** *7*, 015208; doi: 10.1088/2053-1583/ab59a8.
25. Kim, K.; DaSilva, A.; Huang, S.; Fallahazad, B.; Larentis, S.; Taniguchi, T.; Watanabe, K.; LeRoy, B.J.; MacDonald, A.H.; Tutuc, E. Tunable moiré bands and strong correlations in small-twist-angle bilayer graphene. *Proc. Natl. Acad. Sci. USA* **2017**, 114, 3364–3369; doi: 10.1073/pnas.1620140114.
26. Wallbank, J.R.; Kumar, R.K.; Holwill, M.; Wang, Z.; Auton, G.H.; Birkbeck, J.; Mishchenko, A.; Ponomarenko, L.A.; Watanabe, K. Taniguchi, T.; Novoselov, K. S.; Aleiner, I. L.; Geim, A. K.; Fal'ko, V. I. Excess resistivity in graphene superlattices caused by umklapp electron–electron scattering. *Nature Phys.* **2018**, *15*, 32–36; doi: 10.1038/s41567-018-0278-6.
27. Choi, Y.W.; Choi, H.J. Strong electron-phonon coupling, electron-hole asymmetry, and nonadiabaticity in magic-angle twisted bilayer graphene. *Phys. Rev. B* **2018**, *98*, 241412; doi: 10.1106/Phys.Rev.B.241412.
28. Sharpe, A.L.; Fox, E.J.; Barnard, A.W.; Finney, J.; Watanabe, K.; Taniguchi, T.; Kastner, M.A.; Goldhaber-Gordon, D. Emergent ferromagnetism near three-quarters filling in twisted bilayer graphene. *Science* **2019**, *365*, 605–608; doi: 10.1126/science.aaw3780.
29. Polshyn, H.; Yankowitz, M.; Chen, S.; Zhang, Y.; Watanabe, K.; Taniguchi, T.; Dean, C.R.; Young, A.F. Large linear-in-temperature resistivity in twisted bilayer graphene. *Nature Phys.* **2019**, *15*, 1011–1016; doi: 10.1038/s41567-019-0596-3 .
30. Lian, B.; Wang, Z.; Bernevig, B.A. Twisted bilayer graphene: A phonon-driven superconductor. *Phys. Rev. Lett.* **2019**, *122*, 257002; doi: 10.1106/Phys.Rev.Lett.257002.
31. Kerelsky, A.; McGilly, L.J.; Kennes, D.M.; Xian, L.; Yankowitz, M.; Chen, S.; Watanabe, K.; Taniguchi, T.; Hone, J.; Dean, C.; et al. Maximized electron interactions at the magic angle in twisted bilayer graphene. *Nature* **2019**, *572*, 95–100; doi: .
32. Sharpe, A. L. et al. Emergent ferromagnetism near three-quarters filling in twisted bilayer graphene. Science 365, 605–608 (2019).
33. Chu, Y.; Zhu, F.; Wen, L.; Chen, W.; Chen, Q.; Ma, T. Superconductivity in twisted multilayer graphene: A smoking gun in recent condensed matter physics. *Chin. Phys. B* **2020**, *29*, 117401; doi: 10.1088/1674-1056/abbbea.
34. Nimbalkar, A.; Kim, H. Opportunities and Challenges in Twisted Bilayer Graphene: A Review. *Nano-Micro Lett.* **2020**, *12*, 126; doi: 10.1007/s40820-020-00464-8.
35. Serlin, M. et al. Intrinsic quantized anomalous Hall effect in a moiré heterostructure. Science 367, 900–903 (2020).
36. Das, I.; Lu, X.; Herzog-Arbeitman, J.; Song, Z.-D.; Watanabe, K.; Taniguchi, T.; Bernevig, B.A.; Efetov, D.K. Symmetry-broken Chern insulators and Rashba-like Landau-level crossings in magic-angle bilayer graphene. *Nature Phys.* **2021**, *17*, 1-5; doi: 10.1038/s41567-021-01186-3.
37. He, M.; Li, Y.; Cai, J.; Liu, Y.; Watanabe, K.; Taniguchi, T.; Xu, X.; Yankowitz, M. Symmetry breaking in twisted double bilayer graphene. *Nature Phys.* **2021**, *17*, 26–30; doi: 10.1038/s41567-020-1030-6.
38. He, M.; Zhang, Y.-H.; Li, Y.; Fei, Z.; Watanabe, K.; Taniguchi, T.; Xu, X.; Yankowitz, M. Competing correlated states and abundant orbital magnetism in twisted monolayer-bilayer graphene. *Nature Commun.* **2021**, *12*, 4727; doi: 10.1038/s41467-021-25044-1.
39. Li, W.; Reichhardt, C. J. O.; Jankó, B.; Reichhardt, C. Vortex dynamics, pinning, and angle-dependent motion on moiré patterns. *Phys. Rev. B* **2021**, *104*, 024504; doi: 10.1106/Phys.Rev.B.024504.
40. Ledwith, P.J.; Khalaf, E.; Vishwanath, A. Strong coupling theory of magic-angle graphene: A pedagogical introduction. *Annals of Physics* **2021**, *435*, 168646; doi: 10.1016/j.aop.2021.168646.

41. Saito, Y.; Ge, J.; Rademaker, L.; Watanabe, K.; Taniguchi, T.; Abanin, D.A.; Young, A.F. Hofstadter subband ferromagnetism and symmetry-broken Chern insulators in twisted bilayer graphene. *Nature Phys.* **2021**, *17*, 478-481; doi: 10.1038/s41567-020-01129-4.
42. Cao, Y.; Park, J. M.; Watanabe, K.; Taniguchi, T.; Jarillo-Herrero, P. Pauli-limit violation and re-entrant superconductivity in moiré graphene. *Nature* **2021**, *595*, 526-531; doi: 10.1038/s41586-021-03685-y.
43. Hu, C.; Wu, T.; Huang, X.; Dong, Y.; Chen, J.; Zhang, Z.; Lyu, B.; Ma, S.; Watanabe, K.; Taniguchi, T.; Xie, G.; Li, X.; Liang, Q.; Shi, Z. In-situ twistable bilayer graphene. *Sci. Rep.* **2022**, *12*, 204; doi: 10.1038/s41598-021-04030-z.
44. Romanova; M.; Vlček, V. Stochastic many-body calculations of moiré states in twisted bilayer graphene at high pressures. *npj Computational Materials* **2022**, *8*,11; doi: 10.1038/s41524-022-00697-8.
45. Ghawri, B.; Mahapatra, P.S.; Garg, M.; Mandal, S.; Bhowmik, S.; Jayaraman, A.; Soni, R.; Watanabe, K.; Taniguchi, T.; Krishnamurthy, H. R.; Jain, M.; Banerjee, S.; Chandni, U.; Ghosh, A. Breakdown of semiclassical description of thermoelectricity in near-magic angle twisted bilayer graphene. *Nature Commun.* **2022**, *13*, 1522; doi: 10.1038/s41467-022-29198-4.
46. Klein, D.R.; Xia, L.-Q.; MacNeill, D.; Watanabe, K.; Taniguchi, T.; Jarillo-Herrero, P. Electrical switching of a moiré ferroelectric superconductor. *Nature Nanotechnology* **2023**; doi: 10.1038/s41565-022-01314-x.
47. Klebl, L.; Goodwin, Z.A.H.; Mostofi, A.A.; Kennes, D.M.; Lischner, J. Importance of long-ranged electron-electron interactions for the magnetic phase diagram of twisted bilayer graphene. *Phys. Rev. B* **2021**, *103*, 195127; doi: 10.1103/Phys.Rev.B.195127.
48. Vahedi, J.; Peters, R.; Missaoui, A.; Honecker, A.; Trambly, L.G. Magnetism of magic-angle twisted bilayer graphene. *SciPost Phys.* **2021**, *11*, 083; doi: 10.21468/SciPostPhys.11.4.083.
49. Finney, J.; Sharpe, A.L.; Fox, E.J.; Hsueh, C.; Watanabe, K.; Taniguchi, T.; Kastner, M.; Goldhaber-Gordon, D. Unusual magnetotransport in twisted bilayer graphene. *PNAS* **2022**, *119*, e2118482119; doi: 10.1073/pnas.211848211.
50. Decker, R.; Wang, Y.; Brar, V.W.; Regan, W.; Tsai, H.-Z.; Wu, Q.; Gannett, W.; Zettl, A.; Crommie, M. F. Local Electronic Properties of Graphene on a BN Substrate via Scanning Tunneling Microscopy. *Nano Lett.* **2011** *11*, 2291–2295; doi: 10.1021/nl2005115.
51. Wang, L.; Zihlmann, S.; Liu, M.-H.; Makk, P.; Watanabe, K.; Taniguchi, T.; Baumgartner, A.; Schönenberger, Chr. New Generation of Moiré Superlattices in Doubly Aligned hBN/Graphene/hBN Heterostructures. *Nano Lett.* **2019** *19*, 2371–2376; doi: 10.1021/acs.nanolett.8b05061.
52. Hermann, K. Periodic overlayers and moiré patterns: theoretical studies of geometric properties. *J. Phys.: Condens. Matter* **2012** *24*, 314210; doi: 10.1088/0953-8984/24/31/314210.
53. Moon, P.; Koshino, M. Electronic properties of graphene/hexagonal-boron-nitride moiré superlattice. *Phys. Rev. B* **2014** *90*, 155406; doi: 10.1103/PhysRevB.90.155406.
54. Anđelković, M.; Milovanovic, S. P.; Covaci, L.; Peeters, F. M. Double moiré with a twist: super-moiré in encapsulated graphene. *Nano Lett.* **2020** (), 9b04058; doi:10.1021/acs.nanolett.9b04058.
55. Tang, K.; Qi, W. Moiré-Pattern-Tuned Electronic Structures of van der Waals Heterostructures. *Adv. Funct. Mater.* **2020** *2020*, 2002672; doi: 10.1002/adfm.202002672.
56. Martin, I. Moiré superconductivity. *Annals of Physics* **2020** *417*, 116118; doi: 10.1016/j.aop.2020.168118.
57. Xi Zhang, X.; Tsai, K.-T.; Zhu, Z.; Ren, W.; Luo, Y.; Carr, S.; Luskin, M.; Kaxiras, E.; Wang, K. Correlated Insulating States and Transport Signature of Superconductivity in Twisted Trilayer Graphene Superlattices. *Phys. Rev. Lett.* **2021**, *127*, 166802; doi: 10.1103/PhysRevLett.127.166802.
58. Sharpe, A.L. Stacks on stacks on stacks. *Nature Mater.* **2022**, 21, 838–847; doi: 10.1038/s41563-022-01314-1.
59. Park, J.M.; Cao, Y.; Xia, L.; Sun, S.; Watanabe, K.; Taniguchi, T.; Jarillo-Herrero, P. Magic-Angle Multilayer Graphene: A Robust Family of Moiré Superconductors. *Nature Mater.* **2022**, 21, 877–883; doi: 10.1038/s41563-022-01287-1.
60. Burg, G.W.; Khalaf, E.; Wang, Y.; Watanabe, K.; Taniguchi, T.; Tutuc, E. Emergence of correlations in alternating twist quadrilayer graphene. *Nature Mater.* **2022**, 21, 884–889; doi: 10.1038/s41563-022-01286-2.
61. Xie, S.; Faeth, B.D.; Tang, Y.; Li, L.; Gerber, E.; Parzyck, C.T.; Chowdhury, D.; Zhang, Y.-H.; Jozwiak, C.; Bostwick, A.; Rotenberg, E.; Kim, E.-A.; Shan, J.; Mak, K.F.; Shen, K.M. Strong interlayer interactions in bilayer and trilayer moiré superlattices. *Sci. Adv.* **2022**, *8*, eabk1911; doi: 10.1126/sciadv.abk1911.

62. Stanev, V., Oses, C., Kusne, A. G., Rodriguez, E., Paglione, J., Curtarolo, S., Takeuchi, I. Machine learning modeling of superconducting critical temperature. *npj Computational Materials* **2018** *4*, 29, doi:10.1038/s41524-018-0085-8.
63. Matsumoto, K., Horide, T. An acceleration search method of higher T_c superconductors by a machine learning algorithm. *Appl. Phys. Express* **2019** *12*, 073003, doi: 10.7567/1882-9786/ab2822.
64. Zeng, S.; Zhao, Y.; Li,G.; Wang, R.; Wang, X.; Ni, J. Atom table convolutional neural networks for an accurate prediction of compounds properties. *npj Computational Materials* **2019** *5*, 84; https://doi.org/10.1038/s41524-019-0223-y.
65. Hutcheon, M. J.; Alice M. Shipley, A. M.; Richard J. Needs, R. J. Predicting novel superconducting hydrides using machine learning approaches. *Phys. Rev. B* **2020** *101*, 144505; doi: 10.1103/PhysRevB.101.144505.
66. Lee, D.; You, D.; Lee, D.; Li, X.; Kim, S. Machine-Learning-Guided Prediction Models of Critical Temperature of Cuprates. *J. Phys. Chem. Lett.* **2021** *12*, 6211–6217; doi: 10.1021/acs.jpclett.1c01442.
67. Stanev, V.; Choudhary, K.; Kusne, A.G.; Paglione, J.; Takeuchi, I. Artificial intelligence for search and discovery of quantum materials. *Commun. Mater.* **2021**, *2*, 105; doi: 10.1038/s43246-021-00209-z.
68. Roeser, H. P., Hetfleisch, Huber, F. M., Stepper, M., von Schoenermark, M. F., Moritz, A., Nikoghosyan, A. S. A link between critical transition temperature and the structure of superconducting $YBa_2Cu_3O_{7-\delta}$. *Acta Astronautica* **2008** *62*, 733–736; doi: 10.1016/j.actaastro.2008.04.004.
69. Roeser, H. P., Hetfleisch, Huber, F. M., von Schoenermark, M. F., Stepper, M.; Moritz, A., Nikoghosyan, A. S. Correlation between oxygen excess density and critical temperature in superconducting Bi-2201, Bi-2212 and Bi-2223. *Acta Astronautica* **2008** *63*, 1372–1375; doi:10.1016/j.actaastro.2008.06.001.
70. Roeser, H. P., Huber, F. M., von Schoenermark, M. F., Nikoghosyan, A. S. High temperature superconducting with two doping atoms in La-doped Bi-2201 and Y-doped Bi-2212. *Acta Astronautica* **2009** *65*, 489–494, doi:10.1016/j.actaastro.2009.02.004.
71. Roeser, H. P., Haslam, D. T., Hetfleisch, F., Lopez , J. S., von Schoenermark, M. F., Stepper, M., Huber, F. M., Nikoghosyan, A. S. Electron transport in nanostructures: A key to high temperature superconductivity? *Acta Astronautica* **2010** *67*, 546–552, doi:10.1016/j.actaastro.2010.04.014.
72. Roeser, H.P.; Bohr, A.; Haslam, D.T.; López, J.S.; Stepper, M.; Nikoghosyan, A.S. Size quantization in high-temperature superconducting cuprates and a link to Einstein's diffusion law. *Acta Astronaut.* **2012**, *76*, 37–41, doi:10.1016/j.actaastro.2012.04.014.
73. Huber, F.; Roeser, H. P., von Schoenermark, M. A correlation between T_c of Fe-based HT Superconductors and the crystal super lattice constants of the doping element positions. *J. Phys. Soc. Jpn.* **2008** *77* Suppl. C, 142-144; doi: 10.1143/JPSJS.77SC.142.
74. Koblischka, M. R., Roth, S., Koblischka-Veneva, A., Karwoth, T., Wiederhold, A., Zeng, X. L., Fasoulas, S., and Murakami, M. Relation between Crystal Structure and Transition Temperature of Superconducting Metals and Alloys. *Metals* **2020** *10*, 158; doi: 10.3390/met10020158.
75. Koblischka-Veneva, A., Koblischka, M. R. (*RE*)BCO and the Roeser-Huber formula. *Materials* **2021** *14*, 6068; doi: 10.3390/ma14206068.
76. Koblischka, M. R., Koblischka-Veneva, A. Calculation of T_c of superconducting elements with the Roeser-Huber formalism. *Metals* **2022** *12*, 337; doi: 10.3390/met12020337.
77. Ghosh, K. J. B.; Kais, S.; Herschbach, D. R. Dimensional interpolation for metallic hydrogen. *Phys. Chem. Chem. Phys.* **2021** *23*, 7841–7848; doi: 10.1039/d0cp05301e.
78. Mathew, S.; Aben Regi Abraham; Chintalapati, S.; Sarkar, S.; Joseph, B.; Venkatesan, T. Temperature Dependent Structural Evolution of WSe_2: A Synchrotron X-ray Diffraction Study. *Condens. Matter* **2020** *5*, 76; doi:10.3390/condmat5040076.
79. Talantsev, E.F. Quantifying the Charge Carrier Interaction in Metallic Twisted Bilayer Graphene Superlattices. *Nanomaterials* **2021**, *11*, 1306. https://doi.org/10.3390/nano11051306.
80. W. Meissner, and R. Ochsenfeld. Ein neuer Effekt bei Eintritt der Supraleitfähigkeit. Naturwissenschaften 21, 787-788 (1933).
81. W. Buckel, and R. Kleiner, Supraleitung. Grundlagen und Anwendungen, 7th edition, Wiley-VCH, Weinheim, 2013.
82. Koblischka, M. R.; and Wijngaarden, R. J. Magneto-optical investigations of superconductors. *Supercond. Sci. Technol.* **1995** *8*, 199-213; doi: 10.1088/0953-2048/8/4/002.

83. Bending, S.J. Local magnetic probes of superconductors. *Adv. Phys.* **1999**, *48*, 449-535; doi: 10.1080/000187399243437.
84. Koblischka, M.R.; Hartmann, U. Recent advances in magnetic force microscopy. *Ultramicroscopy* **2003**, *97*, 103-112; doi: 10.1016/S0304-3991(03)00034-2.
85. Oral, A.; Bending, S.J.; Henini, M. Real-time scanning Hall probe microscopy. *Appl. Phys. Lett.* **1996**, *69 (9)*, 1324-1326; doi: 10.1063/1.117582.
86. Sonusen, S.; Karci, O.; Dede, M.; Aksoy, S.; Oral, A. Single layer graphene Hall sensors for scanning Hall probe microscopy (SHPM) in 3–300 K temperature range. *Appl. Surf. Sci.* **2014**, *308*, 414–418; doi: 10.1016/j.apsusc.2014.04.191.
87. Anahory, Y.; Naren, H. R.; Lachman, E. O.; Buhbut Sinai, S.; Uri, A.; Embon, L.; Yaakobi, E.; Myasoedov, Y.; Huber, M. E.; Klajn, R.; Zeldov, E. SQUID-on-tip with single-electron spin sensitivity for high-field and ultra-low temperature nanomagnetic imaging. *Nanoscale* **2020**, *12*, 3174; doi: 10.1039/c9nr08578e.
88. Levine, E.V.; Turner, M.J.; Kehayias, P.; Hart, C.A.; Langellier, N.; Trubko, R.; Glenn, D. R.; Fu, R.R.; Walsworth, R.L. Principles and techniques of the quantum diamond microscope. *Nanophotonics* **2019**, *8(11)*, 1945–1973; doi: 10.1515/nanoph-2019-0209.
89. Hong, S.; Grinolds, M.S.; Pham, L.M.; Le Sage, D.; Luan, L.; Walsworth, R.L.; Yacoby, A. Nanoscale magnetometry with NV centers in diamond. *MRS Bull.* **2013**, *38*, 155-161; doi: 10.1557/mrs.2013.23.
90. Wenzhao Li, W.; Reichhardt, C. J. O.; Jankó, B.; Reichhardt, C. Vortex dynamics, pinning, and angle-dependent motion on moiré patterns. *Phys. Rev. B* **2021**, *104*, 024504; doi: 10.1103/PhysRevB.104.024504.
91. Gorter, C. J.; Casimir, H. On supraconductivity I. *Physica* **1934** *1*, 306–320.
92. Poole, C. P. Jr.; Creswick, R. J.; Farach, H. A.; Prozorov, R. Superconductivity. (Elsevier, UK, Second edition, 2007).
93. Talantsev, E. F.; Crump, W. P.; Island, J. O.; Xing, Y.; Sun, Y.; Wang, J.; Tallon, J. L. On the origin of critical temperature enhancement in atomically thin superconductors. *2D Materials* **2017**, *4*, 025072; doi: 10.1088/2053-1583/aa6917.
94. Pal, B. Pal, B. ; Joshi, B. P. ; Chakraborti, H. ; Jain, A. K. ; Barick, B. K. search by orcid ; Ghosh, K. search by orcid ; Bhunia, S. ; Laha, A.; Dhar, S. ; Gupta, K. Das Experimental evidence of a very thin superconducting layer in epitaxial indium nitride. *Supercond. Sci. Technol.* **32**, 015009; doi: 10.1088/1361-6668/aaed8f .
95. Helfand, E.; Werthamer, N. R. Temperature and purity dependence of the superconducting critical field, H_{c2}. II. *Phys. Rev.* **1966**, *147*, 288-294; doi: 10.1103/PhysRev.147.288.
96. Werthamer, N. R., Helfand, E.; Hohenberg, P. C. Temperature and purity dependence of the superconducting critical field, H_{c2}. III. Electron spin and spin-orbit effects. *Phys. Rev.* **1966**, *147*, 295-302; doi: 10.1103/PhysRev.147.295.
97. Baumgartner, T.; Eisterer, M.; Weber, H. W.; Flükiger, R.; Scheuerlein, C.; Bottura, L. Effects of neutron irradiation on pinning force scaling in state-of-the-art Nb_3Sn wires. *Supercond. Sci. Technol.* **2014**, *27*, 015005;doi: 10.1088/0953-2048/27/1/015005.
98. Jones, C. K., Hulm, J. K.; Chandrasekhar, B. S. Upper critical field of solid solution alloys of the transition elements. *Rev. Mod. Phys.* **1964**, *36*, 74–76 (1964); doi: 10.1103/RevModPhys.36.74.
99. Talantsev, E. F. DC self-field critical current in superconductor/Dirac-cone material/superconductor junctions. *Nanomaterials* **2019**, *9*, 1554; doi:10.3390/nano9111554.
100. Koblischka-Veneva, A.; Koblischka, M. R. High-T_c Cuprate Superconductors: Materials, Structures and Properties. In: *Superconducting Materials. Fundamentals, Synthesis and Applications*; Slimani, Y.; Hannachi, E.; Springer-Nature, Singapore, 2022, Chap. 7, pp. 181-210.
101. Talantsev, E.F. Critical de Broglie wavelength in superconductors. *Mod. Phys. Lett. B* **2018**, *32*, 1850114; doi: 10.1142/S0217984918501142.
102. Rohlf, J. W.: Modern Physics from α to Z^0. Wiley, New York (1994).
103. Mori, N.; Wilson, J. A.; Ozaki, H. Fluctuation conductivity in the 110-K phase of Ni-doped (Bi,Pb)-Sr-Ca-Cu-O superconductors. *Phys. Rev. B* **1992** *45*, 10633–10638; doi: 10.1103/PhysRevB.45.10633.
104. Larkin, A.; Varlamov, A. Fluctuation Phenomena in Superconductors. Oxford University Press, Oxford, U.K., 2005.

105. Koblischka, M. R.; Koblischka-Veneva, A.; Zeng, X. L.; Hannachi, E.; Slimani, Y. Microstructure and Fluctuation-Induced Conductivity Analysis of $Bi_2Sr_2CaCu_2O_{8+\delta}$ (Bi-2212) Nanowire Fabrics. *Crystals* **2020** *10*, 986; doi:10.3390/cryst10110986.
106. Uemura, Y. J.; Le, L. P.; Luke, G. M.; Sternlieb, B. J.; Wu, W. D.; Brewer, J. H.; Riseman, T. M.; Seaman, C. L.; Maple, M. B.; Ishikawa, M.; Hinks, D. G.; Jorgensen, J. D.; Saito, G.; Yamochi, H. Basic Similarities among Cuprate, Bismuthate, Organic, Chevrel-Phase, and Heavy-Fermion Superconductors Shown by Penetration Depth Measurements. *Phys. Rev. Lett.* **1991** *66*, 2665–2668; doi: 10.1103/PhysRevLett.66.2665.
107. Uemura, Y. J. Condensation, excitation, pairing, and superfluid density in high-T_c superconductors: the magnetic resonance mode as a roton analogue and a possible spin-mediated pairing. *J. Phys.: Condens. Matter* **2004**, *16*, S4515–S4540; doi: 10.1088/0953-8984/16/40/007.
108. Harshman, D. R.; Fiory, A. T. High-T_c Superconductivity Originating from Interlayer Coulomb Coupling in Gate-Charged Twisted Bilayer Graphene Moiré Superlattices. *J. Supercond.* **2020** *33*, 367-378; doi: 10.1007/s10948-019-05183-9.
109. Xiao, Y.; Liu, J.; Fu, L. Moiré is More: Access to New Properties of Two-Dimensional Layered Materials. *Matter* **2020**, *3*, 1142–1161, doi: 10.1016/j.matt.2020.07.001.
110. Boochani, A.; Jamal, M.; Shahrokhi, M.; Nowrozi, B.; Gholivand, M.B.; Khodadadi, J.; Amiri, M.; Asshabia, M.; Yaria, A. Ti_2VGe Heuslerene: theoretical prediction of a novel 2D material. *J. Mater. Chem. C* **2019**, *7*, 13559; doi: 10.1039/c9tc03176f.
111. Wang, T.; Noah, F.; Yuan, Q.; Fu, L. Moiré Surface States and Enhanced Superconductivity in Topological Insulators. *Phys. Rev. X* **2021**, *11*, 021024; doi: 10.1103/PhysRevX.11.021024.
112. Kezilebieke, S.; Vano, V.; Huda, Md N.; Aapro, M.; Ganguli, S.C.; Liljeroth, P.; Lado, J.L. Moiré-Enabled Topological Superconductivity. *Nano Lett.* **2022**, *22*, 328-333; doi: 10.1021/acs.nanolett.1c03856.